Measurement of electrons from beauty-hadron decays in *pp* and Pb-Pb collisions at $\sqrt{s_{NN}} = 5.02$ TeV

S. Acharya *et al.*[*]
(ALICE Collaboration)

(Received 16 December 2022; accepted 25 July 2023; published 15 September 2023)

The production of electrons from beauty-hadron decays was measured at midrapidity in proton-proton (pp) and central Pb-Pb collisions at center-of-mass energy per nucleon-nucleon pair $\sqrt{s_{NN}} = 5.02$ TeV, using the ALICE detector at the LHC. The cross section measured in pp collisions in the transverse momentum interval $2 < p_{\mathrm{T}} < 8\,\mathrm{GeV}/c$ was compared with models based on perturbative quantum chromodynamics calculations. The yield in the 10% most central Pb-Pb collisions, measured in the interval $2 < p_{\mathrm{T}} < 26\,\mathrm{GeV}/c$, was used to compute the nuclear modification factor R_{AA}, extrapolating the pp reference cross section to p_{T} larger than 8 GeV/c. The measured R_{AA} shows significant suppression of the yield of electrons from beauty-hadron decays at high p_{T} and does not show a significant dependence above $8\,\mathrm{GeV}/c$ within uncertainties. The results are described by several theoretical models based on different implementations of the interaction of heavy quarks with a quark-gluon plasma, which predict a smaller energy loss for beauty quarks compared to light and charm quarks.

DOI: 10.1103/PhysRevC.108.034906

I. INTRODUCTION

The formation of a strongly coupled color-deconfined medium, called quark-gluon plasma (QGP), is predicted by quantum chromodynamics (QCD) calculations on the lattice at high energy density and temperature [1–5]. These extreme conditions can be created in ultrarelativistic heavy-ion collisions, which were used to establish the formation of the QGP and to study its properties [6,7] at the SPS [8,9], RHIC [10–13], and LHC [14,15] accelerators.

Heavy quarks (charm and beauty) are predominantly produced in the initial hard-scattering processes [16], given that their mass is large compared to the thermal energy scale ($m_{c,b} \gg k_B T_{\mathrm{QGP}}$, where k_B is the Boltzmann constant and T_{QGP} is the temperature of the QGP) and on a timescale shorter than the QGP formation time [17] ($\tau_{\mathrm{QGP}} \approx 1\,\mathrm{fm}/c$ [18]). Their mass is also large compared to the QCD scale Λ_{QCD}, allowing perturbative calculations of their production cross section to be applicable down to zero transverse momentum (p_{T}) [19–22]. Given the early production of heavy quarks during the collision, they experience all the stages of the system evolution [17,23]. They interact with the medium constituents via both elastic (collisional) and inelastic (gluon radiation) processes [24–29], where the relative contribution of the latter increases with p_{T}. As the heavy quarks from the early collision rarely annihilate or get produced thermally [17,30,31], the effect of the interactions with the medium is primarily a change in the momentum distribution of the quarks. Quarks moving faster than the surrounding medium are typically slowed down by the interactions (resulting in in-medium energy loss), while slow quarks may get accelerated and pushed along with the surrounding medium. Measuring the effect of these interactions yields insights into the transport properties of the QGP [17]. The interaction of partons with the medium is expected to depend on the color charge and the mass of the parton [25–27,32], with a stronger interaction of gluons compared to quarks and of lighter quarks compared to heavier ones for both collisional and radiative processes. The mass dependence of the radiative contribution is connected to the dead-cone effect [25,33], which predicts gluon radiation to be suppressed for angles $\theta \leqslant m/E$, where m and E are the mass and energy of the quark. The measurement of hadron species with different quark contents over a large p_{T} range is therefore fundamental to shed light on the underlying mechanisms of the in-medium quark energy loss. Measurements of hadrons containing beauty quarks (beauty hadrons) are particularly useful for testing the mass dependence of the parton energy loss up to high transverse momenta.

The effect of the medium is usually quantified using the nuclear modification factor R_{AA}, defined as the ratio between the p_{T}-differential particle yields in nucleus-nucleus (A-A) collisions (dN_{AA}/dp_{T}) and the corresponding production cross section in pp collisions ($d\sigma_{pp}/dp_{\mathrm{T}}$) at the same energy scaled by the average nuclear overlap function $\langle T_{AA} \rangle$ for the centrality range under study [34,35]

$$R_{AA} = \frac{1}{\langle T_{AA} \rangle} \frac{dN_{AA}/dp_{\mathrm{T}}}{d\sigma_{pp}/dp_{\mathrm{T}}}. \tag{1}$$

The production cross section of beauty hadrons and their decay products in hadronic collisions has been measured at

[*]Full author list given at the end of the article.

different energies at RHIC [36,37], Tevatron ($p\overline{p}$) [38], and at the LHC [15,39–54]. These measurements are described by perturbative quantum chromodynamics (pQCD) calculations such as fixed order plus next-to-leading-log (FONLL) [19–21] and general-mass variable flavor-number scheme (GM-VFNS) [22] within uncertainties.

The interaction of heavy quarks with the medium can be studied via the measurement of charm hadrons, which can be reconstructed using their exclusive hadronic decays. Measurements in Pb-Pb collisions show a significant change in their momentum distribution with respect to pp collision data [55–57]. Together with measurements of the flow coefficients [58–62], this can provide significant constraints to models of the transport properties of the QGP medium [15,23,55,63]. To investigate the quark-mass dependence of the interaction, measurements in the beauty sector are needed as well. Due to the small cross section of beauty-hadron production and their large number of decay channels, the full reconstruction of beauty hadrons is difficult in heavy-ion collisions. While it is possible to reconstruct beauty hadrons, as for example in the $B^{\pm}$ measurement through the decay channel $B^{\pm} \to J/\psi + K^{\pm} \to \mu^{+}\mu^{-} + K^{\pm}$ [41,45,48,64,65] with a BR of $(6.12 \pm 0.19) \times 10^{-5}$ [66], the small branching ratios make such measurements challenging. Complementary information can be gained using inclusive measurements of beauty-hadron decay products such as nonprompt J/ψ [47,67,68], nonprompt D mesons [52,69–71], or through leptons originating from semileptonic decays of heavy-flavor hadrons [72–76]. The nuclear modification factor of leptons from beauty-hadron decays has been measured by the ALICE collaboration for semielectronic decays in Pb-Pb collisions at $\sqrt{s_{NN}} = 2.76\,\text{TeV}$ [72] and for semimuonic decays at $\sqrt{s_{NN}} = 5.02\,\text{TeV}$ with $p_{\text{T}} > 4\,\text{GeV}/c$ [77], while the elliptic flow coefficient has been measured at $\sqrt{s_{NN}} = 5.02\,\text{TeV}$ by the ALICE [78] and ATLAS [79] collaborations. The measurement of leptons from heavy-flavor decays can provide information about a large range of hadron and heavy-quark momenta, which can help to gain an understanding about the interplay of the collisional and radiative processes.

In this article, the ALICE measurements of the p_{T}-differential cross section of electrons from beauty-hadron decays in pp collisions at $\sqrt{s} = 5.02$ TeV, the p_{T}-differential yield in the 10% most central Pb-Pb collisions at $\sqrt{s_{NN}} = 5.02$ TeV, and the corresponding nuclear modification factor at midrapidity are presented. The results are discussed together with a comparison to theoretical models.

II. EXPERIMENTAL APPARATUS AND DATA SAMPLES

The ALICE apparatus consists of a central barrel covering the pseudorapidity region $|\eta| < 0.9$ and a muon spectrometer with $-4 < \eta < -2.5$ coverage. It also contains forward- and backward-pseudorapidity detectors employed for triggering, background rejection, and event characterization. The nominal magnetic field, parallel to the beam axis and provided by the solenoid magnet in which the central barrel detectors are placed, is 0.5 T. A complete description of the detector and an overview of its performance are presented in Refs. [80,81].

The central-barrel detectors used in the analyses presented in this article for charged-particle reconstruction and electron identification at midrapidity are the inner tracking system (ITS) [82], the time projection chamber (TPC) [83], the time-of-flight (TOF) [84] detector, and the electromagnetic calorimeter (EMCal) [85]. The ITS consists of six layers of silicon detectors, with the innermost two composed of silicon pixel detectors (SPD), two intermediate layers of silicon drift detectors, and the two outermost layers made of double-sided silicon strip detectors. The ITS is used to reconstruct the primary vertex and for tracking charged particles, the latter in combination with the TPC. The SPD crucially also provides very good spatial resolution down to low transverse momentum, important requirement for the analyses presented in this paper. The TPC is the main tracking detector of the central barrel. In addition, it allows for particle identification via the measurement of the particle specific energy loss (dE/dx) in the detector gas. Additional information for particle identification is provided by the TOF [84], via the measurement of the charged-particle flight time from the interaction point to the detector. The event collision time is determined using the TOF itself or the two T0 arrays [86], made of quartz Cherenkov counters and covering the acceptance $4.6 < \eta < 4.9$ and $-3.3 < \eta < -3.0$. The EMCal detector [85,87] is a shashlik-type lead and scintillator sampling electromagnetic calorimeter [88] that covers an acceptance of $|\eta| < 0.7$ in pseudorapidity and $\Delta\varphi = 107^{\circ}$ in azimuth. The smallest segmentation of the EMCal is a tower, which has a dimension of $6 \times 6\,\text{cm}^2$ ($0.0143 \times 0.0143\,\text{rad}^2$) in the $\eta \times \phi$ direction. The EMCal is used for electron identification as well as for triggering on rare events with high momentum particles in its acceptance.

Two scintillator arrays (V0) [89], placed on each side of the interaction point (with pseudorapidity coverage $2.8 < \eta < 5.1$ and $-3.7 < \eta < -1.7$), are used to define a minimum-bias trigger, to reject offline beam-induced background events, and for event characterization. The V0 detectors along with the two T0 arrays are employed to measure the cross section corresponding to the minimum-bias trigger condition [90]. The zero degree calorimeters [91] located at 112.5 m on both sides of the interaction point are used to reject electromagnetic interactions and beam-induced background in Pb-Pb collisions.

The heavy-ion collisions were divided into different centrality classes using the signal of the V0 detectors [92,93]. The centrality refers to the percentile of the hadronic cross section covered, with lower values corresponding to more central events.

The results presented in this paper were obtained using data recorded by ALICE during the LHC Run 2 data-taking period in 2017 for pp collisions at center-of-mass energy $\sqrt{s} = 5.02$ TeV and in 2015 for Pb-Pb collisions at center-of-mass energy per nucleon-nucleon collision $\sqrt{s_{NN}} = 5.02$ TeV. To obtain a uniform acceptance of the detectors, only events with a reconstructed primary vertex position along the beam line located within ± 10 cm from the center of the detector were considered for both pp and Pb-Pb collisions. Additionally, events were selected after standard quality checks on the performance of the detectors used in the analyses. The

analysis in pp collisions was performed using the minimum bias (MB) trigger, which requires coincident signals in both scintillator arrays of the V0 detector. In Pb-Pb collisions, the analysis using TPC and TOF detectors was based on a MB triggered sample, while the TPC-EMCal analysis employed the MB and a high-energy event trigger based on the energy deposited in the EMCal. The EMCal trigger (EG) is based on the sum of energy in a sliding window of 4×4 towers above a given threshold, where the required energy threshold for the Pb-Pb data sample was 10 GeV above the background energy from the underlying event. The background from the underlying event was obtained using the median of 16×16 tower patches in the opposite side calorimeter referred to as DCAL. The analyzed number of MB events is 930×10^6 in pp collisions corresponding to an integrated luminosity of $L_{\rm int} = 18.2 \pm 0.4\,{\rm nb}^{-1}$ [94], and 6.7×10^6 and 4.8×10^6 events for the 10% most central Pb-Pb collisions for the TPC–TOF and TPC–EMCal analysis, corresponding to integrated luminosities of $L_{\rm int} = 8.9 \pm 0.2\,\mu{\rm b}^{-1}$ and $6.2 \pm 0.1\,\mu{\rm b}^{-1}$ [92], respectively. The number of analyzed EMCal triggered events is 57×10^4 in the 10% most central Pb-Pb collisions, corresponding to an integrated luminosity of $45.6 \pm 3.6\,\mu b^{-1}$.

III. ANALYSIS OVERVIEW

Throughout this paper, the term "electron" is used for indicating both electrons and positrons. In the momentum range $p_{\rm T} \geqslant 2\,{\rm GeV}/c$ considered in these analyses, most of the electrons produced near the interaction vertex at midrapidity come from the decays of heavy-flavor hadrons [95]. They can be produced directly or as part of the decay chain. Other processes producing electrons that constitute a background in the measurement of electrons from heavy flavor decays are Dalitz and dielectron decays of light mesons (π^0, η, ρ, ω, η', ϕ), photon conversions in the detector material, decays of hadrons containing strange quarks, decays of prompt quarkonia, and decays of vector bosons. For these, the decay chains of heavier particles may also contain lighter electron sources (e.g., $K^0_S \to \pi^0\pi^0$). Generally, such contributions are more significant at low $p_{\rm T}$.

The measurements of electrons from beauty-hadron decays can be broadly split into four steps: (i) track selection, (ii) electron identification, (iii) signal extraction to estimate the fraction of electrons originating from beauty-hadron decays, and (iv) a correction for selection efficiencies and geometrical acceptance.

Good quality tracks were selected using the criteria detailed in Sec. III A. The electron identification (eID) was performed in two different ways depending on the particle $p_{\rm T}$. At low $p_{\rm T}$ ($2 < p_{\rm T} < 8\,{\rm GeV}/c$) in pp and Pb-Pb collisions, the eID was based on the combination of signals of the TPC and TOF detectors. In Pb-Pb collisions, a second analysis was performed in the interval $3 < p_{\rm T} < 26\,{\rm GeV}/c$ exploiting the combined eID information from TPC and EMCal. The TPC-EMCal analysis was performed using MB triggered events for the $p_{\rm T}$ interval $3 < p_{\rm T} < 12\,{\rm GeV}/c$ and using EMCal triggered events for $12 < p_{\rm T} < 26\,{\rm GeV}/c$ to profit from the substantially larger integrated luminosity sampled with this trigger in a momentum interval in which the EG trigger selection is fully efficient. For the final results, the yields obtained from TPC-EMCal analysis were used for $p_{\rm T} > 8\,{\rm GeV}/c$, whereas the overlapping region of $3 < p_{\rm T} < 8\,{\rm GeV}/c$ was used to check the consistency between the TPC–TOF and TPC–EMCal measurements. This choice was motivated by the precision of the measurement based on statistical and systematic uncertainties, as will be further discussed in Sec. IV.

The signal of electrons from beauty-hadron decays was separated from the other background electron sources via an analysis of the track impact parameter (d_0) distribution, exploiting the comparatively longer lifetime of beauty hadrons ($c\tau \approx 500\,\mu{\rm m}$ [96]) with respect to other electron sources. The d_0 is defined as the distance of closest approach of the electron track to the reconstructed interaction vertex in a plane perpendicular to the beam direction. It has a positive or negative sign depending on whether the track passes on the left or right of the primary vertex. This value was multiplied by the sign of the charge of the track and by the sign (direction) of the magnetic field along the z axis.

The signal was extracted through a Monte Carlo (MC) template fit of the d_0 distribution, using four templates in the case of the TPC-TOF analysis and two templates in the TPC-EMCal analysis as described in Secs. III C and III D, respectively.

A. Track selection and electron identification

The track selection has two main goals: assuring high-quality tracks and reducing the contribution of background electrons. In particular, requiring hits in detectors close to the interaction point removes part of the contribution of electrons from photon conversions that occur in the detector material. For the analyses based on TPC-TOF, all tracks were required to have an associated hit in each of the two innermost layers of the ITS. In the high-track-density environment of a central Pb-Pb collision, it is however possible for a track produced at a larger radius by a photon conversion to be associated with the hits of another particle in the inner layers. These are referred to as misassociated conversion electrons. To reduce this contribution, tracks were required to have at most one hit in the ITS which is shared with another track. For the TPC-EMCal analysis, the tracks were required to have at least one hit in one of the two innermost layers of the ITS. This reduces the impact of the inactive channels in the first ITS layer in the acceptance window of the EMCal.

The TPC track quality is ensured by several selections on the clusters associated to the track, reported in Table I. In particular, the tracks are required to have a minimum total number of clusters and a minimum fraction of found clusters relative to the expected maximum considering the track position in the detector geometry (found/findable). Additional requirements on the number of crossed pad rows are applied as in Ref. [97].

The resulting resolution of the impact parameter of the selected tracks with $p_{\rm T} > 2$ GeV/c is better than 60 μm for the pp measurement, 50 μm for the TPC-EMCal analysis in Pb-Pb, and 40 μm for TPC-TOF in Pb-Pb. The complete list of selection criteria can be found in Table I and is similar to earlier analyses [95].

TABLE I. Selection criteria for electron candidates.

	pp TPC-TOF	Pb-Pb TPC-TOF	Pb-Pb TPC-EMCal
Rapidity	$\lvert y\rvert < 0.8$	$\lvert y\rvert < 0.8$	$\lvert y\rvert < 0.6$
DCA_z	<2 cm	<2 cm	<1 cm
TPC clusters for tracking	–	$\geqslant 100$	$\geqslant 80$
TPC crossed rows for tracking	$\geqslant 70$	–	$\geqslant 70$
TPC clusters for dE/dx	$\geqslant 80$	$\geqslant 80$	–
found/findable clusters	–	>0.6	–
crossed rows/findable clusters	>0.8	–	>0.8
max. χ^2 per cluster in TPC	4	4	4
max. χ^2 per cluster in ITS	36	5	36
number of ITS clusters	$\geqslant 4$	$\geqslant 4$	$\geqslant 3$
number of SPD hits	2	2	1 or 2
number of shared ITS clusters	–	at most 1	–
ITS and TPC refit	yes	yes	yes
Reject kink daughters	yes	yes	yes
TPC-EMCal matching	–	–	$\lvert\Delta\eta\rvert < 0.05, \lvert\Delta\varphi\rvert < 0.05$
TPC eID signal	$-1 < n_{\sigma,e}^{\mathrm{TPC}} < 3$	$-0.16 < n_{\sigma,e}^{\mathrm{TPC}} < 3$	$-1 < n_{\sigma,e}^{\mathrm{TPC}} < 3$
TOF eID signal	$\lvert n_{\sigma,e}^{\mathrm{TOF}}\rvert < 3$	$\lvert n_{\sigma,e}^{\mathrm{TOF}}\rvert < 3$	–
EMCal E_{cal}/p	–	–	$0.8 < E_{\mathrm{cal}}/p < 1.2$
EMCal shower shape	–	–	$0.01 < \sigma^2_{\mathrm{short}} < 0.35$

For electron identification with the TPC (TOF), the measured signal was compared to the expected signal for electrons. The selection was performed on the variables $n_{\sigma,e}^{\mathrm{TPC}}(n_{\sigma,e}^{\mathrm{TOF}})$, defined as the deviation of the signal from the expectation for an electron in units of the expected resolution. For the EMCal, the main variable used for separating electrons from hadrons was E_{cal}/p: the deposited energy (E_{cal}) in the calorimeter divided by the reconstructed particle momentum (p), together with information about the shape of the electromagnetic shower. The shower shape is characterized by the eigenvalues of the dispersion matrix of the shower shape ellipse defined by the energy distribution within the EMCal cluster [87,98,99]. In this analysis, it was chosen to require the short axis of the ellipse, $\sigma^2_{\mathrm{short}}$ [100], within the range $0.01 < \sigma^2_{\mathrm{short}} < 0.35$, to reduce the hadron contamination. The lower threshold of $\sigma^2_{\mathrm{short}}$ was chosen to reduce the contamination caused by neutrons hitting the readout electronics. All the eID selection criteria can be found in Table I. The low but finite remaining hadron contamination was explicitly estimated and subtracted in the method employing TPC and EMCal. It was considered as part of the impact parameter fit in the measurements based on TPC and TOF as discussed in Sec. III E 1.

B. Impact parameter distributions of the different electron sources

The electron candidates originate from different sources, as described in Sec. III. As part of the separation is based on the track impact parameter, it is useful to consider the different shapes of the impact parameter distributions. Electrons from beauty-hadron decays have a particularly wide impact parameter distribution due to the large decay length of the hadrons ($c\tau \approx 500\,\mu$m [96]). For the electrons from charm-hadron decays this distribution is somewhat narrower ($40 < c\tau < 300\,\mu$m [96]) though still wide compared to many of the other background contributions. Light mesons like neutral pions can decay to electrons directly via three-body Dalitz decays, accounting for a significant portion of the light meson background. As these decays, similar to those of quarkonia and vector bosons, essentially occur at the interaction vertex, their impact parameter distribution is narrow and is determined by the reconstructed track resolution. Light mesons can also produce electrons via decays to photons that convert in the detector material. Electrons originating from photon conversions have a very small angle with respect to the photon direction. However, due to the magnetic field, the track acquires a sizable average impact parameter when it is propagated back to the primary vertex with opposite sign for positrons and electrons. Multiplying the impact parameter with the sign of the track charge and magnetic field orientation makes the distribution asymmetric, making it easier to distinguish it from the other sources. Most of the electrons from photon conversions at large radii are removed by the requirement of signals in the inner ITS layers. The few remaining misassociated conversion electrons have a very wide impact parameter distribution. Most of the hadrons left in the sample after electron identification are produced near the interaction vertex. Thus, their impact parameter distribution is similar to that of the Dalitz decay electrons.

The electrons from Dalitz decays and the photons converting in the detector material mostly come from the decays of light-flavor particles, and are produced in electron–positron pairs with low invariant mass. Together, the electrons from these two sources are referred to as "photonic electrons."

The analyses presented here extract the beauty and charm contributions with a fit of the inclusive track impact parameter distribution using templates based on event and detector simulations. The approaches using TPC and TOF detectors also include the conversion electrons and remaining sources as

templates and will be referred to as the four-template method. The photonic electron contribution, which decreases with p_{T}, can be subtracted before fitting the d_0 distributions utilizing a technique based on electron–positron pairs with low invariant mass. This approach, referred to as the two-template method, was used in the analysis with the particle identification based on the TPC and EMCal detectors. These methods will be discussed in more detail in the following sections. One effect of the subtraction of the photonic electrons is that it also subtracts a contribution from light mesons produced in the decays of beauty hadrons. The four-template method, instead, includes all electrons produced in the decay chains of beauty hadrons. This was estimated to induce a difference between the results of the two analysis techniques, which is of the order of 2% in the measured p_{T} range and decreases with p_{T}.

The fit templates, as well as the estimation of the tracking and part of the eID efficiencies, are based on MC simulations. The PYTHIA v6.425 event generator with Perugia 2011 tune [101] was used to simulate pp events, HIJING v1.36 [102] for Pb-Pb events, while GEANT3 [103] was used to propagate the generated particles through the ALICE apparatus. The conditions of all the ALICE detectors during the data taking, were taken into account in the simulations. Simulated events were enriched with additional electrons from beauty- and charm-hadron decays as well as decays of π^0 and η mesons to improve the statistical precision for the signal and the main background sources. Any deviation between the MC templates and the data was corrected whenever possible and any uncertainty in the correction was propagated to the systematic uncertainties of the measurement. Corrections were applied for the transverse impact parameter resolution, the momentum distribution of the charm and beauty hadrons, and the relative fractions of the different charm-hadron species (which impacts on the d_0 templates because of the significantly different decay lengths of D^0, D^+, D_{s}^+, Λ_{c}^+). Due to the free amplitudes of the contributions in the fit, only effects on the shape of the impact parameter distributions are relevant, not the total number of entries in the templates. Effects of including electrons from strange-hadron decays, the dependence of the conversion electron distribution on the detector occupancy, and the relative contribution of the hadron contamination were considered as systematic uncertainties. These are discussed in more detail in Sec. III E.

C. Extraction of electrons from beauty-hadron decays using the four-template method

In this approach, four impact parameter templates for the corresponding electron sources discussed in the previous section are constructed based on MC simulations and are fitted to the measured inclusive electron distribution using a maximum likelihood fit approach. The template corresponding to contributions that are from neither beauty, charm, nor photon conversions will be referred to as the Dalitz template. This procedure was applied in the p_{T} interval $2 < p_{\mathrm{T}} < 8\,\mathrm{GeV}/c$ with an electron identification based on the signals of the TOF and TPC detectors.

The signal extraction is based on the method of fitting finite-statistics templates proposed in Ref. [104] and was already used in previous ALICE analyses [72]. The basic idea is to include the fluctuations in the templates by introducing the expectation values A_{ji} of the templates of source j in bin i as free parameters in addition to the overall amplitudes. The contributions from the sources are then estimated from the overall maximum likelihood assuming Poissonian fluctuations.

Corrections for the fractions of the different charm-hadron species and for the momentum distributions of the charm and beauty hadrons were included via weights of the different entries in the impact parameter histograms. Profiting from the free amplitude parameters, all scaling functions can be changed by an overall multiplicative factor. This was used to keep the weights to values close to unity to not disrupt the Poisson statistics assumed in the maximum likelihood fit. For electrons from beauty- and charm-hadron decays, the uncertainties from statistical fluctuations in the templates are much lower than those on the measured distribution (by around a factor of 3).

Examples for the resulting fit together with the scaled template distributions in pp and Pb-Pb collisions are shown in Fig. 1. The ratio of the data to the fit, is also shown to demonstrate the quality of the fit, which is around 1 in the full d_0 range considered for the fit. Due to the large decay length, the contribution from beauty-hadron decays is most prominent at large absolute impact parameter values and this region thus constrains the magnitude of the beauty contribution the most. The statistical uncertainty of the fit was determined by virtually repeating the measurement using independent samples created from the templates based on measured contributions as input as in Ref. [72]. In addition to the distinct electron sources, there is also a contribution from the remaining hadron contamination. As these hadrons mostly originate near the interaction vertex, the contribution is absorbed into the fit of the Dalitz decay electron contribution.

The slight difference in the average impact parameter and its resolution between data and the simulations used to create the templates was estimated via the measurement of charged hadron tracks and corrected for. The remaining resolution difference is <4% and was considered as a part of the systematic uncertainties.

Electrons from the decay of heavy-flavor hadrons within a particular p_{T} interval can originate from different hadron species (e.g., D^0, D^+, D_{s}^+, Λ_{c}^+ for charm hadrons and B^0, B^+, B_{s}^0, Λ_B^0 for beauty hadrons, as well as their antiparticles) with different lifetimes and also with a wide range of possible momenta. Thus, the impact parameter distributions depend on the momentum distributions and relative abundances of charm and beauty hadrons. In particular, the charm hadrons have significantly different lifetimes. To correct for this effect, electrons from charm-hadron decays were weighted by the species and momenta of their mothers according to the measured D^0 momentum distributions and the measured $\Lambda_{\mathrm{c}}^+/D^0$ [105,106], D^+/D^0 [55,107], and D_s^+/D^0 [57,107] yield ratios, to obtain the MC templates. For beauty, the weights for the p_{T}-distributions of the beauty hadrons were estimated according to FONLL calculations for the p_{T} distributions using an additional correction for the nuclear modification factor based on the TAMU model [108] in the Pb-Pb analysis. As all beauty hadrons have a similar decay length and thus the

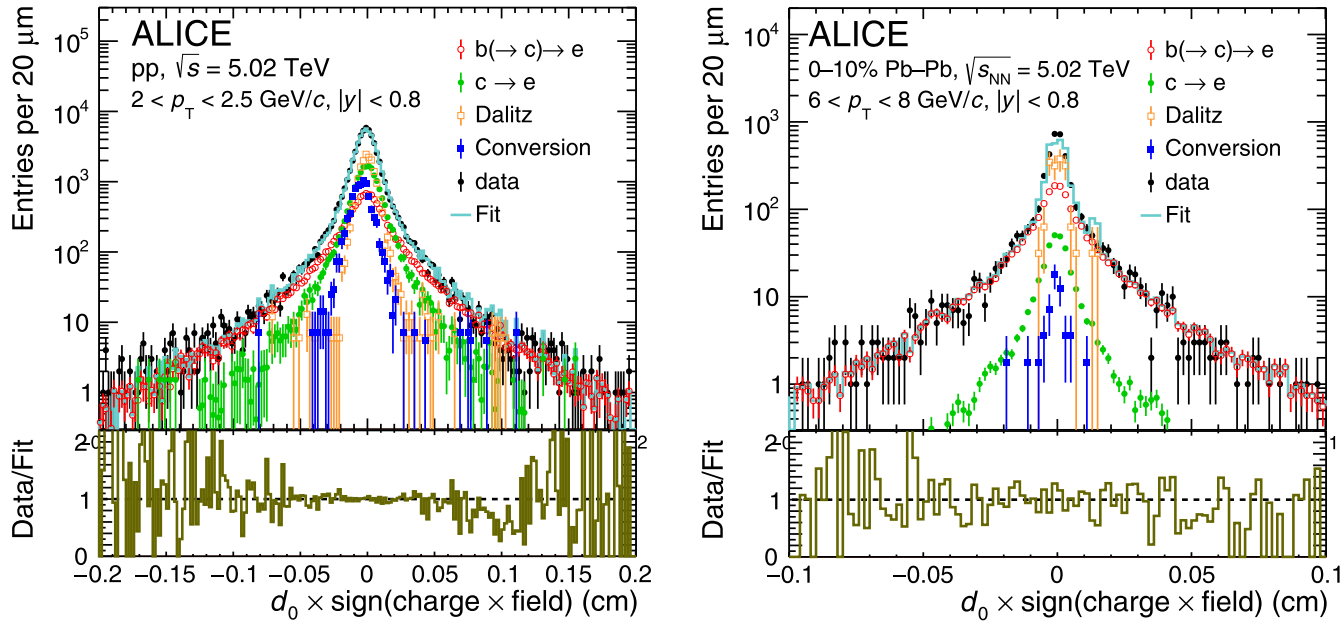

FIG. 1. Examples of the impact parameter fits with the four-template fit approach used in the TPC–TOF analyses. The left panel shows a fit with templates for the four classes of electron sources in pp collisions at $\sqrt{s} = 5.02$ TeV in the lowest p_T interval and the right panel shows a fit example in Pb-Pb collisions at $\sqrt{s_{NN}} = 5.02$ TeV in the highest p_T range.

corresponding decay electrons are expected to have similar impact parameter distributions, no specific correction was made for the relative contributions of the different beauty hadrons.

The number of measured particles was then taken from the integral of the scaled fit templates after performing the fitting procedure. It was then corrected for the acceptance of the ALICE detector (ε^{geo}) and the efficiency of the electron reconstruction ($\varepsilon^{\text{reco}}$) and identification ($\varepsilon^{\text{eID}}$) and normalized to the number of events according to Eq. (2). A factor of $\frac{1}{2}$ is included to give the average of electrons and positrons,

$$\frac{d^2\text{N}}{dp_T dy} = \frac{1}{2}\frac{1}{\Delta y \Delta p_T}\frac{1}{N_{\text{events}}}\frac{N_{\text{raw}}}{\varepsilon^{\text{geo}} \times \varepsilon^{\text{reco}} \times \varepsilon^{\text{eID}}}. \quad (2)$$

The efficiency for the track-quality and TOF eID selections was estimated from MC simulations. For the TPC eID efficiency, a data-driven technique which is based on a fit of the $n_{\sigma,e}^{\text{TPC}}$ distribution after TOF eID, was used for all momentum intervals. The electron peak was fitted using a Gaussian distribution. The resulting mean was around -0.16 for all momentum intervals in Pb-Pb collisions. A selection of $n_{\sigma,e}^{\text{TPC}}$ from -0.16 to 3 was applied, resulting in a constant TPC eID efficiency of about 50%. The small correction for the finite transverse momentum resolution was done via a bin-by-bin correction comparing generated and measured momenta in the simulations.

D. Extraction of electrons from beauty-hadron decays using the two-template method

In the second procedure, the contributions from hadrons and photonic electrons are subtracted from the d_0 distribution through data-driven methods similar to the ones used in Ref. [109]. The contributions of electrons from charm- and beauty-hadron decays are then determined by fitting the d_0 distribution with two templates, one for charm and one for beauty sources, obtained from MC simulations. This method was used in the Pb-Pb analysis using eID based on the TPC and EMCal detectors in the p_T range from 3 to 26 GeV/c. The inclusive electron sample was obtained by selecting tracks and by applying electron identification criteria in the TPC and the EMCal using $n_{\sigma,e}^{\text{TPC}}$, E_{cal}/p, and σ^2_{short}, as listed in Table I.

1. Data-driven background subtraction

The hadron contamination was estimated by selecting hadron tracks with $n_{\sigma,e}^{\text{TPC}} < -4$. The E_{cal}/p distribution of these particles was then scaled to match the electron-candidate E_{cal}/p distribution in an interval that varies with p_T inside the range $0.2 < E_{\text{cal}}/p < 0.6$. This hadron E_{cal}/p normalization range shifts with increasing p_T to account for the shift of the hadron signal towards $E_{\text{cal}}/p = 1$ with increasing momentum. The electron- and hadron-contamination yields were obtained by integrating the E_{cal}/p distributions of electron candidates and the scaled hadron one in $0.8 < E_{\text{cal}}/p < 1.2$. The hadron contamination is negligible at low p_T, and increases to around 20% at $p_T = 26$ GeV/c. The hadron d_0 distribution, obtained by selecting particles with $n_{\sigma,e}^{\text{TPC}} < -4$, was also scaled to match this estimated hadron contamination. It was then subtracted from the inclusive electron d_0 distribution (dN^{InclE}/dd_0).

After the subtraction of the hadron contamination, the contribution of photonic electrons was estimated. Photonic electrons are produced in electron-positron pairs with low invariant mass, peaking close to zero. Thus, they can be identified using an invariant mass analysis of electron pairs. In the invariant mass analysis technique [110,111], electron-positron pairs are defined by pairing the selected electrons

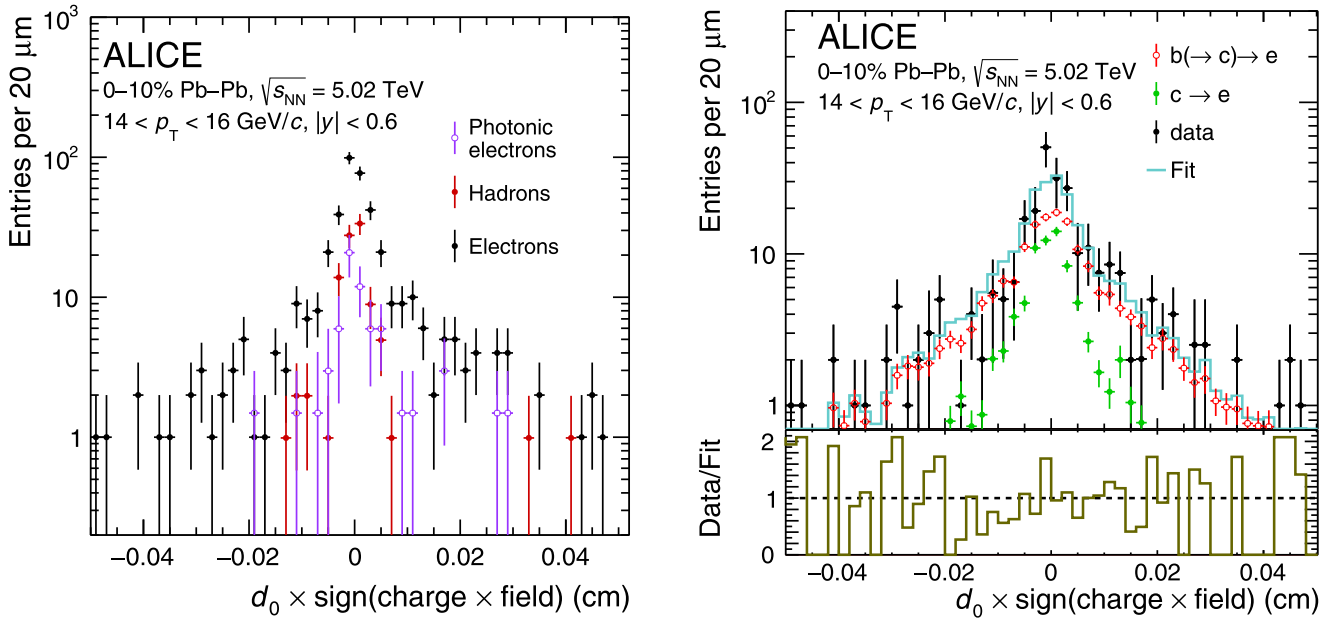

FIG. 2. Example of the impact parameter distributions used in the TPC–EMCal analysis in 0–10% Pb-Pb collisions at $\sqrt{s_{NN}} = 5.02$ TeV. The hadron contamination (red), photonic electron (purple), and inclusive electron (black) d_0 distributions are shown in the left panel. The right panel shows an example of a fit with the two template approach.

with opposite-charge electron partners to form unlike-sign (ULS) pairs and calculating their invariant mass ($m_{e^+e^-}$). The partner electrons were selected by applying similar but looser track quality and particle identification criteria than those used for selecting signal electrons to increase the efficiency of finding the partner [111,112]. Heavy-flavor decay electrons can form ULS pairs mainly through random combinations with other electrons. The combinatorial contribution was estimated from the invariant mass distribution of like-sign electron (LS) pairs. The d_0 distributions of electrons forming ULS ($dN^{\rm ULS}/dd_0$) and LS ($dN^{\rm LS}/dd_0$) pairs were obtained. The photonic background contribution was then evaluated by subtracting the LS distribution from the ULS distribution in the invariant mass interval $m_{e^+e^-} < 0.1\,{\rm GeV}/c^2$. The efficiency of finding the partner electron, referred to as the tagging efficiency ($\varepsilon_{\rm tag}$) from here on, was estimated using the HIJING [102] MC simulations with added light flavor signals at high momenta. The generated particles are propagated through the ALICE apparatus using GEANT3 [103]. The simulated $p_{\rm T}$ distributions of π^0 and η mesons were reweighted to match the unbiased $p_{\rm T}$ distribution from PYTHIA. The tagging efficiency is ≈50% at 3 GeV/c, increasing to ≈70% at $p_{\rm T} > 20\,{\rm GeV}/c$. The d_0 distribution of photonic electrons was corrected for with the tagging efficiency and subtracted from the inclusive electron distribution to obtain the impact parameter distribution of electrons from heavy flavor hadron decays ($dN^{\rm HFe}/dd_0$) according to

$$\frac{dN^{\rm HFe}}{dd_0} = \frac{dN^{\rm InclE}}{dd_0} - \frac{1}{\varepsilon_{\rm tag}}\left(\frac{dN^{\rm ULS}}{dd_0} - \frac{dN^{\rm LS}}{dd_0}\right). \quad (3)$$

An example of the d_0 distribution of inclusive electrons, estimated hadron contamination, and photonic electrons is shown in the left panel of Fig. 2 for the interval $3 < p_{\rm T} < 4\,{\rm GeV}/c$.

Electrons from strange-hadron decays are negligible in the $p_{\rm T}$ range considered [95]. The contribution of electrons from J/ψ decays was estimated to be less than 5% with a maximum at $2 < p_{\rm T} < 3\,{\rm GeV}/c$ [111,112], hence not considered in the analysis. The $W^{\pm}$ (Z^0) boson decays have a negligible contribution for $p_{\rm T} < 15\,{\rm GeV}/c$, increasing to 20% (10%) of the heavy-flavor decay electron yield at $p_{\rm T} = 26\,{\rm GeV}/c$ [109]. These contributions were not subtracted but their small effect on the yield is considered in the systematic uncertainty estimation, as described below.

2. *Two-template fit procedure*

The electrons from beauty-hadron decays were separated by fitting two MC d_0 templates to the heavy-flavor electron d_0 distribution, using a procedure similar to that detailed in Sec. III C. The two templates correspond to electrons from charm-hadron decays and beauty-hadron decays.

Several corrections were applied to the MC d_0 templates of charm- and beauty-hadron decays to obtain a realistic description of the data, before using them to fit the measured distributions. These corrections include (i) the $p_{\rm T}$ shape of the mother charm and beauty hadrons, (ii) the relative fraction of the different charm-hadron mother species, and (iii) the mean and the resolution of the d_0 distribution. The corrections were applied using the same procedure described in Sec. III C.

The corrected MC templates of charm and beauty decays were used to fit the heavy-flavor electron d_0 distribution from data using a weighted log-likelihood fit [113]. The statistical uncertainties from the templates were not considered in the fit, as the statistical uncertainties of the data dominate over those of the templates (approximately six times larger). An example

TABLE II. Systematic uncertainties in the pp and Pb-Pb analyses. Individual sources of systematic uncertainties are p_{T} dependent. The values are presented as a range corresponding to the lowest and highest p_{T} intervals.

Source	pp TPC-TOF $2 < p_{\mathrm{T}} < 8\,\mathrm{GeV}/c$	Pb-Pb TPC-TOF $2 < p_{\mathrm{T}} < 8\,\mathrm{GeV}/c$	Pb-Pb TPC-EMCal $3 < p_{\mathrm{T}} < 26\,\mathrm{GeV}/c$
Track selection	1%	3%	2%
ITS-TPC matching	2%	3%	3%
TPC-TOF matching	2%	5%	–
TPC-EMCal matching	–	–	1%
TPC eID	1%	7%	–
TOF eID	4%–0%	7%–2%	–
TPC-EMCal eID	–	–	7%–10%
IP resolution	6%	5%–0%	2%
Charm-hadron p_{T} spectra	2%–0%	5%–2%	1%–5%
Charm-hadron species	4%–0%	1%–0%	5%
Beauty-hadron p_{T} spectra	10%–5%	10%–5%	10%–3%
Hadron contamination	0%–10%	8%–4%	1%–3%
Fit stability	10%–0%	5%–0%	0%
Strangeness decay contribution	–	3%–1%	–
Partner electron selection	–	–	2%–0%
Multiplicity effect for conversions	–	4%–1%	–
Fit method	20%	15%	15%
Closure test	–	–	20%–4%
W/Z contribution	–	–	0%–6%
EMCal trigger rejection factor	–	–	0%–5%
Total	26%–23%	26–18%	28–22%
Normalization uncertainty	2.1%	–	–

of a fit is shown in the right panel of Fig. 2 for the interval $14 < p_{\mathrm{T}} < 16\,\mathrm{GeV}/c$. The ratio of the data to the fit is also shown to demonstrate the quality of the fit. It is around 1 in the full d_0 range considered for the fit.

The raw beauty-decay electron yield obtained from the template fit was then corrected for the acceptance of the ALICE detector and the efficiency of the electron reconstruction and identification as described by Eq. (2). This includes the efficiency corrections for the track quality selections, the procedure to match tracks with EMCal energy-deposition clusters, and the selections used to identify electrons (the E_{cal}/p, $\sigma^2_{\mathrm{short}}$, and $n^{\mathrm{TPC}}_{\sigma,e}$ requirements). The efficiencies were estimated using MC simulations, with the exception of the $n^{\mathrm{TPC}}_{\sigma,e}$ and $\sigma^2_{\mathrm{short}}$ electron selection efficiencies, which was estimated using data-driven procedures.

The $n^{\mathrm{TPC}}_{\sigma,e}$ efficiency was estimated by parametrizing the $n^{\mathrm{TPC}}_{\sigma,e}$ distributions by fitting with three Gaussians, for the electron, the pion, and the combined proton and kaon signals. The obtained efficiency varies from about 72% to 76% with increasing momentum. The relative efficiency of $\sigma^2_{\mathrm{short}}$ was obtained using E_{cal}/p distribution with and without applying the shower shape selection. The resulting efficiency varies from about 80% to 95% with increasing momentum.

The per-event yield obtained with EMCal-triggered events for $p_{\mathrm{T}} > 12\,\mathrm{GeV}/c$ was normalized using the EMCal trigger rejection factor. The rejection factor expresses the equivalent number of MB events corresponding to a triggered event. It was estimated with a data-driven method, using the ratio of the EMCal cluster energy distribution in EG-triggered data to the one in minimum-bias data (EG/MB), similar to what is described in Refs. [109,111]. This ratio forms a stable plateau above $E_{\mathrm{cluster}} > 12\,\mathrm{GeV}/c$. A Fermi function [114,115] was used to fit the ratio and to determine the EMCal trigger rejection factor above the trigger threshold. A rejection factor of $61.7 \pm 0.8(\mathrm{stat.}) \pm 3.0(\mathrm{sys.})$ was obtained. The statistical uncertainty was obtained by varying the fit function within its parameter uncertainties, and the systematic uncertainty was obtained by changing the fit function using a constant above the trigger threshold, and also varying the fit range. The uncertainty on the EMCal trigger rejection factor was propagated to the final measurement.

E. Systematic uncertainties

1. Systematic uncertainty estimation for the four-template method

The systematic uncertainties in pp and Pb-Pb collisions with TPC–TOF eID are summarized in Table II. They can broadly be separated into uncertainties on the estimate of the efficiency of the track selection and eID and uncertainties related to the shape of the fit templates. The different sources of uncertainties were assumed to be uncorrelated and thus added in quadrature. For the calculation of the R_{AA}, they were considered as uncorrelated between pp and Pb-Pb. A detailed description of the contributions is given in the following.

The systematic uncertainty for the track quality selection efficiency in pp and Pb-Pb collisions is 1% and 3%, respectively, for electrons from beauty- and charm-hadron decays as estimated in Ref. [109] from variations of the selection criteria. The uncertainty estimated for heavy-flavor decay electrons in Ref. [109] can be applied in the analysis presented

here because, at a given p_{T}, tracks of electrons from beauty-hadron decays have similar properties as tracks of those from charm-hadron decays and therefore the systematic uncertainty due to track reconstruction and selection is the same. The systematic uncertainty due to the imperfect description in the MC of the efficiency of matching tracks reconstructed in the ITS and TPC, is about 2% in pp and about 3% in Pb-Pb collisions [109].

Charged particle tracks reconstructed in the TPC have to be matched with TOF hits, to compute the time of flight for particle identification. The detector acceptance does not depend on particle species, thus charged particles can be used to calculate the matching efficiency between TPC and TOF. The systematic uncertainty on the TPC-TOF matching efficiency was obtained by comparing the matching efficiency of charged particles in data and MC and was estimated to be 2% and 5% in pp and Pb-Pb collisions, respectively [109].

The TPC and TOF eID uncertainties were estimated using a pure sample of electrons produced in photon conversions in the detector material, selected according to the corresponding decay topology (V0 electrons). Since both electrons from beauty-hadron decays and V0 electrons produced in the ITS give the same detector signals in the outer layers, the latter can be used as a proxy to investigate the differences of the eID efficiency between data and simulation. For Pb-Pb collisions, the systematic uncertainty on the TPC eID was estimated to be of 7% in all p_{T} intervals from the difference between data and MC. For the analysis in pp collisions, where the TPC signal shape is easier to model than in central Pb-Pb collisions [72], the model for the extraction of the efficiency was varied, leading to a change of around 1% in efficiency which was added as a systematic uncertainty. The TOF eID systematic uncertainties reach a maximum of 7% in the lowest p_{T}-interval and a minimum of 2% in the highest p_{T}-interval for Pb-Pb collisions while the range is 4% to 0% in pp collisions.

The correction for differences in the d_0 resolutions and in the average of the d_0 distribution between data and simulations extracted for charged-particle tracks was applied to improve the description of the data on average for all particles, independent of the species. Thus, depending on the specific track selection criteria, some deviations can still be present. The relative residual deviation was smaller than 4% for the impact parameter resolution. A systematic uncertainty of 6% over the entire p_{T} range was estimated for pp collisions by varying the resolution correction accordingly, while for Pb-Pb collisions the effect was 5% for $p_{\mathrm{T}} < 5\,\mathrm{GeV}/c$ and negligible at larger p_{T}.

The uncertainties from the correction of the parent hadron p_{T} distribution for electrons from charm-hadron decays originate from the uncertainty of the measurements used as input for the corrections. As the fit has a free amplitude parameter, the correction does not depend on the integrated yield of the measurement, but mostly on its p_{T} shape. To account for this, the correction was modified by tilting the measured D^0 [107] spectrum based on its total uncertainty. The uncertainty was then estimated by comparing the fit results for beauty-hadron decay electrons using the different corrections. An uncertainty of 2% was assigned in pp collisions for electron p_{T} below 6 GeV/c. In Pb-Pb collisions, a systematic uncertainty of 5% was assigned below 5 GeV/c and 2% above. The uncertainty due to the unknown relative abundances of the different charm-hadron species was estimated by varying the Λ_c^+/D^0 [105,106], D^+/D^0 [55,107], and D_s^+/D^0 [57,107] ratios within the statistical and systematic uncertainties of the measurements, and assessing the effect of these variations on the yield of electron from beauty-hadron decays. The uncertainty for pp is 4% for $p_{\mathrm{T}} < 2.5$ GeV/c, 2% for $2.5 < p_{\mathrm{T}} < 5$ GeV/c, and negligible above. For Pb-Pb it is 1% for $p_{\mathrm{T}} < 3$ GeV/c and negligible above.

For the beauty case, the input p_{T} shapes from the considered models were varied. In the Pb-Pb case, the most effective variation on the model is the change of the R_{AA} slope. Two large variations were tested, adding and subtracting half the distance of the R_{AA} to unity to the central values. The resulting beauty-hadron decay electron yields were compared to the central correction to estimate the systematic uncertainty due to the beauty-hadron p_{T} spectrum. In Pb-Pb collisions, a systematic uncertainty of 10% was assigned below 3 GeV/c and 5% above. For the pp measurement, the estimation was based on the uncertainties of the FONLL pQCD calculation. To estimate the corresponding uncertainties, the upper and lower limits of the FONLL calculations were used as alternative weights. In this way, the systematic uncertainties on the beauty-hadron decay electron yield reach a maximum of 10% in the lowest p_{T} interval and a minimum of 5% in the highest p_{T} interval in pp collisions.

Despite the stringent eID selections, some hadron contamination remains in the selected electron sample. Since pions are abundant and the TPC signals for electrons and pions overlap at high p_{T}, the hadron contamination is mostly due to charged pions. In Pb-Pb collisions the hadron contamination contributes over the entire p_{T} range, while in pp collisions it is only significant at high p_{T}, similarly as reported in Ref. [109]. To investigate the effect of the hadron contamination, the template fit was repeated, replacing the Dalitz template by the hadron template obtained from data by requiring $-5 < n_{\sigma,e}^{\mathrm{TPC}} < -3$. The impact parameter distributions of these two templates are similar because Dalitz electron sources and the charged pions originate mostly from the primary vertex. The differences are mainly due to the resolution of the impact parameter for electrons and pions. From the fit with the hadron templates, the measured yield of the beauty-hadron decay electrons varies by about 8% (4%) below (above) 2.5 GeV/c. These values were assigned as the systematic uncertainty in the Pb-Pb analysis. In the pp case, where the TPC signal shape is easier to model, the hadron contamination was estimated using fits of the TPC signal as described in Ref. [95]. The hadron impact parameter distribution template was scaled accordingly and subtracted from the total. The difference in the yield of beauty-hadron decay electrons was assigned as a systematic uncertainty yielding no significant change at low p_{T} and 10% in the range $5 < p_{\mathrm{T}} < 8\,\mathrm{GeV}/c$.

The results of the fits to the impact parameter distributions should be mostly independent of the fit range used as well as of the bin width of the templates used for the different sources. For the Pb-Pb case, such variations showed no clear effect on the result, with a possible effect of <5% found only in the first p_{T} interval below 2.5 GeV/c. In pp, an effect is

visible below 2 GeV/c, which decreases with p_{T}. Varying the fit range between $|d_0| < 0.1$ and $|d_0| < 0.2$ and the bin width in the range 5 μm to 20 μm gives an effect on the beauty decay electron yield of the order of ≈10% in 2–2.5 GeV/c and ≈5% up to 5 GeV/c. These values were added as systematic uncertainties.

The electron candidates include contributions from secondary π^0 decays and three body decays of strange hadrons which have a wide impact parameter distribution. The effect of these secondary tracks on the Dalitz and conversion electron templates was investigated by varying the fraction of this contribution. Based on the results of charged pions and kaons [116], the secondary contribution in the Dalitz and conversion electron templates was scaled by factors 3 and 0 to estimate the effect on the fitted yield. Considering both variations, the extracted yield of beauty-hadron decay electrons varies from 3% at 2 GeV/c down to 1% at 8 GeV/c in Pb-Pb collisions. The effect of the secondary tracks in pp collisions is negligible.

The shape of the impact parameter distribution of electrons from photon conversions depends on the influence of the misassociated conversion electrons. The misassociation probability is approximately proportional to the multiplicity of the event. As a result, the misassociated conversion electron contribution is particularly important to consider in central Pb-Pb collisions. Using conversion electron templates from the centrality range 10–30% instead of the nominal 0–10% corresponds to a change in multiplicity by a factor of about 1.6. The corresponding extracted beauty contribution changes only by 4% for $2 < p_{\mathrm{T}} < 2.5$ GeV/c, decreasing down to 1% in the highest p_{T} range ($6 < p_{\mathrm{T}} < 8$ GeV/c).

The two approaches, TPC-EMCal eID with the two-template fit method and the TPC-TOF eID with the four-template fit method were compared in the overlap region of the analyses and also with a separate test in pp collisions. Comparisons with different eID, centrality, and track selection criteria show a consistent deviation of the order of 15% in Pb-Pb (20% in pp). Typically, the approach using the four-template fit gives a higher yield for electrons from beauty-hadron decays than that of two-template fit. Closer inspection of the systematic effects showed that variations in the assumed d_0 resolution typically lowered the result of the four-template TPC–TOF approach. On the other hand, the effect of additional background electrons from the primary vertex (e.g., from J/ψ decays) would increase the result for the two-template approach. However, both effects together still do not cover the full difference. To account for this, an additional systematic uncertainty of 15% in Pb-Pb and 20% in pp collisions was added.

2. *Systematic uncertainty estimation for the two-template method*

The systematic uncertainties for the approach using the two-template fits originate in the efficiency correction, the background subtraction, and the signal extraction. A summary of all the sources of systematic uncertainty and the assigned values can be found in Table II.

The uncertainty due to track selection was estimated by varying the track selection criteria [109] and was found to be about 2%. The uncertainty from the imperfect description in the MC of the efficiency of matching tracks reconstructed in the ITS and TPC is about 2%. An uncertainty of 1% was estimated for matching electron tracks in the TPC to EMCal clusters by varying the matching criteria. The uncertainty on electron identification using the TPC and the EMCal was estimated by varying the selection criteria on $n_{\sigma,e}^{\mathrm{TPC}}$, E_{cal}/p, and $\sigma^2_{\mathrm{short}}$. These variations test the procedure of removing the hadron contamination and estimating the efficiency. The chosen variations change the efficiency by a maximum of ≈20% while still allowing reasonable signal extraction. A total uncertainty from these sources of 7% for $p_{\mathrm{T}} < 12$ GeV/c and 10% for higher p_{T} was estimated. The E_{cal}/p interval used to normalize the hadron E_{cal}/p distribution to match the electron one in the background region was varied, and the effect on the hadron subtraction method was checked. The scale factor was also varied within its statistical uncertainty. The effect of these variations is more pronounced at high p_{T} where the hadron contamination is larger. The uncertainty due to hadron contamination was estimated to be 1% for $p_{\mathrm{T}} < 12$ GeV/c and 3% for higher p_{T}.

The contribution from photonic electrons was estimated using the invariant mass method. The systematic uncertainty on the procedure, mainly affecting the average correction efficiency, was obtained by varying the selection criteria of the partner electron tracks, including the minimum p_{T} and the invariant-mass window of the electron–positron pairs. While the average tagging efficiency from γ, π^0, and η was used in the analysis, any differences in the efficiency between the different photonic electron sources, estimated using MC simulations, were also considered as a systematic uncertainty. The resulting systematic uncertainty on the yield of beauty-hadron decay electrons is 2% for $3 < p_{\mathrm{T}} < 4$ GeV/c and negligible for $p_{\mathrm{T}} > 4$ GeV/c.

While the uncertainty on the yield of the photonic electrons was obtained using the procedure described above, there can also be an effect from the shape of their d_0 distribution. This can be present if there is a difference between the impact parameter distribution of the photonic electron candidates selected via the invariant mass and that of all photonic electrons in the sample of selected tracks. The corresponding effect on the estimated yield of electrons from beauty-hadron decays was evaluated using a MC closure test. Electrons from photon conversions in the detector material have a d_0 shape that depends on the production vertex, with wider distributions for electrons produced at larger radii. The d_0 distribution from the invariant mass method gives a combination of contributions from Dalitz decays, produced at the primary vertex, and γ conversion processes, which occur at different radii in the detector material. In the MC closure test, the beauty yield was obtained using the data-analysis procedure on simulated data, with realistic fractions of electrons from charm, beauty, and photonic background obtained from previous measurements [109]. The photonic electrons were subtracted using the invariant mass method and the resulting d_0 distribution of candidate heavy-flavor decay electrons was fitted with charm and beauty templates. The beauty yield from the fit was compared to the true input beauty yield in MC simulations, and their difference which was ≈20% at 3 GeV/c

decreasing to 4% at 23 GeV/c, was taken as a systematic uncertainty.

As described in the previous section, the contribution of electrons from $W^{\pm}$ and Z^0 boson decays is nonnegligible for $p_{\mathrm{T}} > 15\,\mathrm{GeV}/c$ and estimated to be ≈30% of the yield of heavy-flavor decay electrons at $p_{\mathrm{T}} = 26\,\mathrm{GeV}/c$ [109]. The effect of this contribution was also studied using a MC closure test, where the d_0 distribution of Dalitz electrons was used as a proxy for $W^{\pm}$ and Z^0 decays, as they both decay close to the primary vertex and the difference is less than the detector resolution of the d_0 distribution. The d_0 distribution of electrons from $W^{\pm}$ decays was added to that of heavy-flavor decay electrons in the simulated sample, which was then fitted using only the charm and beauty templates. The beauty yield obtained from the fit was compared to the true beauty yield to estimate any difference. The maximum difference was 2% for $16 < p_{\mathrm{T}} < 20\,\mathrm{GeV}/c$ rising to 6% for the highest p_{T} interval, and was added as a systematic uncertainty.

The stability of the weighted log-likelihood fit was studied by changing the histogram bin sizes and the fit ranges. The effect on the beauty yield from the fitting routine was found to be negligible.

The uncertainty on the impact parameter resolution was estimated as described in Sec. III E 1, and a value of 2% was assigned.

As discussed in Sec. III C, the d_0 templates of charm- and beauty-hadron decays were obtained using MC simulations after several corrections. The systematic effect of these corrections on the yield of electrons from beauty-hadron decays was assessed by varying the weights applied on the D and B hadron p_{T} spectra, and varying the ratio of different charm-hadron species, in the same way as for the four-template approach. The uncertainty from the assumed beauty hadron p_{T}-distribution results in a systematic uncertainty of 10% for $p_{\mathrm{T}} < 6\,\mathrm{GeV}/c$ and 3% for higher p_{T}. The uncertainty from the charm-hadron p_{T} distributions was obtained by varying the slope of the D-meson p_{T} spectra within the statistical and systematic uncertainty of the D-meson measurement [107] and ranges from 1% for p_{T} up to 20 GeV/c to 5% for the highest p_{T} interval. The uncertainty due to the relative abundances of the different charm-hadron species in the MC, obtained by varying the Λ_c^+/D^0 [105,106], D^+/D^0 [55,107], and ${D_s}^+/D^0$ [57,107] fractions within the statistical and systematic uncertainty of the measurements, was estimated to be 5% over the entire p_{T} range.

As described for the four-template method, an additional uncertainty of 15% was assigned to account for differences in the results of the two methods, estimated in their overlap region ($3 < p_{\mathrm{T}} < 8\,\mathrm{GeV}/c$).

IV. RESULTS

The p_{T}-differential production cross section of electrons from beauty-hadron decays in pp collisions at $\sqrt{s} = 5.02$ TeV, measured at midrapidity in the transverse momentum interval $2 < p_{\mathrm{T}} < 8\,\mathrm{GeV}/c$, is shown in Fig. 3. Vertical error bars depict the statistical uncertainties while the systematic uncertainties are shown by rectangular boxes. The cross section is compared with pQCD calculations such as FONLL

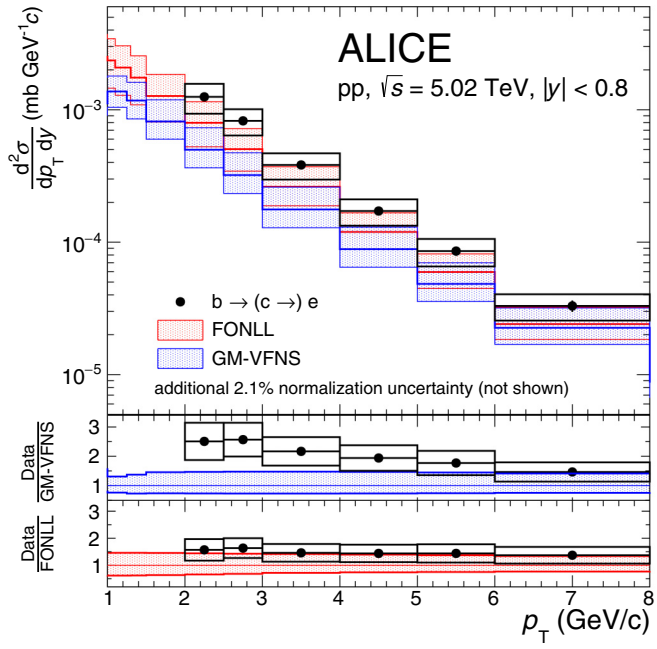

FIG. 3. p_{T}-differential cross section of electrons from beauty-hadron decays in pp collisions at $\sqrt{s} = 5.02$ TeV using TPC-TOF for electron identification. In the upper panel, the cross section is compared with FONLL [19–21] and GM-VFNS [22] predictions. The ratios of data to these calculations are reported in the bottom panels.

[19–21] and GM-VFNS [22]. For the prediction of the p_{T} distribution of leptons from beauty-hadron decays, FONLL calculations use a numerical convolution of a perturbative cross section with a nonperturbative fragmentation function and a decay function for the hadron weak decay into a lepton [21]. The parameters of the fragmentation function are determined from e^+e^- collision data using B^+, B^-, and B^0 mesons. The weak decay function and the branching ratios are also extracted from experimental data. As the fragmentation functions are determined using only B mesons, possible differences in the fragmentation and the decay kinematics of the substantial contribution from beauty baryons [117] are not considered in FONLL calculations. The uncertainty bands of the FONLL calculations are the result of different choices for the mass of beauty quarks, and for the factorization and renormalization scales as well as the uncertainty on the set of parton distribution functions (PDF) used in the pQCD calculations. In the GM-VFNS approach, the contribution of electrons from beauty-hadron decays is calculated from the convolution of the hard-scattering cross section at the partonic level, a nonperturbative fragmentation function, the total beauty-hadron decay width, and the decay spectrum to leptons. The nonperturbative fragmentation functions were obtained based on e^+e^- data using all B mesons (B^+, B^-, and B^0) and Λ_B [22]. The decay width and the spectrum were obtained using the electron energy spectrum in inclusive beauty-meson decays measured by the BABAR experiment [118]. The theoretical uncertainty of the GM-VFNS calculations was obtained by varying the scale parameters related to renormalization and to the factorization of initial- and final-state singularities. The

uncertainties due to scale variation are the dominating source and hence PDF-related uncertainties and variations of the bottom mass were not considered. It should be noted that the results using the four-template method in pp and Pb-Pb collisions include a small contribution ($\approx$2%) of beauty-hadron decays via light mesons, which is not included in the signal definition of the pQCD calculations. The data lies on the upper edge of the FONLL uncertainty band, around a factor 1.5 above the central prediction, similarly to earlier measurements in pp collisions at $\sqrt{s} = 7$ TeV [39]. The measurement using semimuonic decays from the ATLAS collaboration [77] shows a similar behavior in the p_{T} interval common between ALICE and ATLAS, though it is close to the FONLL central value for $p_{\mathrm{T}} > 10\,\mathrm{GeV}/c$. The comparison of FONLL with the previous measurement of nonprompt D mesons [52], however, shows the center of the theory prediction closer to the data. This difference in the FONLL description of beauty decay electrons and nonprompt D mesons could be due to the contribution from beauty baryons. The beauty baryons produce electrons with a similar branching ratio, and decay kinematics as beauty mesons. However, the branching ratio of beauty baryons into D mesons is smaller than that for beauty mesons. Since all beauty quarks are assumed to fragment into mesons in the FONLL calculations, the nonprompt D meson contribution would be increased relative to the electrons. Comparison of the results to GM-VFNS predictions shows some tension for $p_{\mathrm{T}} < 4\,\mathrm{GeV}/c$. In the second p_{T} interval the central point of the measurement is about 1.9σ above the upper edge of the GM-VFNS uncertainty band when considering the combined statistical and systematic uncertainties of the measurement. At higher p_{T}, the predictions are in closer agreement between each other and the data. A qualitatively similar result was found previously for nonprompt D mesons [52]. The models differ in their assumptions concerning the fragmentation functions and the transition to a fixed-flavor number scheme, which should make differences more apparent at low momenta [119].

The measured cross section in pp collisions at $\sqrt{s} =$ 5.02 TeV in Fig. 3 was used as a reference to calculate the R_{AA} up to $p_{\mathrm{T}} = 8\,\mathrm{GeV}/c$. For $p_{\mathrm{T}} > 8\,\mathrm{GeV}/c$, the FONLL prediction for electrons from beauty-hadron decays in pp collisions at $\sqrt{s} = 5.02$ TeV was used. Since the FONLL central prediction is lower than the data at low momentum, the FONLL reference was scaled to match the data. The scaling factor was determined by taking the ratio between the measured cross section and the FONLL prediction for $p_{\mathrm{T}} < 8\,\mathrm{GeV}/c$. This ratio reaches a plateau for $p_{\mathrm{T}} > 4\,\mathrm{GeV}/c$, and was assumed to be constant at higher momenta where the data points are unavailable. The scale factor of 1.40 ± 0.08 was determined by fitting the ratio with a constant for $p_{\mathrm{T}} > 4\,\mathrm{GeV}/c$. The statistical and systematic uncertainties of the measurement were propagated to obtain the systematic uncertainty associated with the scaling factor, assuming no correlation between p_{T} intervals for the statistical uncertainties and full correlation for the systematic ones. The total uncertainty assigned to the scaled FONLL reference is calculated by taking the sum in quadrature of the uncertainty from the original FONLL prediction and the systematic uncertainty of the scaling, and is approximately 30% for $p_{\mathrm{T}} > 8\,\mathrm{GeV}/c$. The result of the extrapolation, scaled with the nuclear overlap function, is shown in Fig. 4.

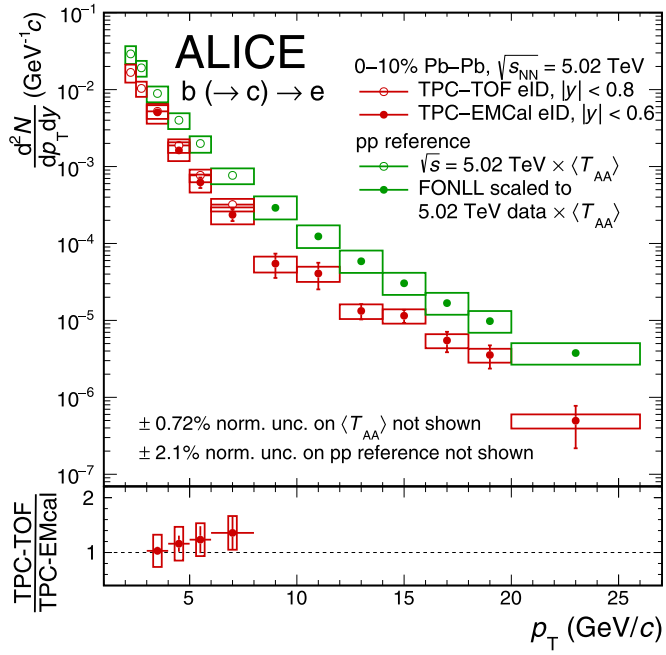

FIG. 4. Yield of beauty-hadron decay electrons in 0–10% central Pb-Pb collisions at $\sqrt{s_{NN}} = 5.02$ TeV for the TPC–TOF and TPC-EMCal analyses compared with the pp reference scaled by $\langle T_{AA} \rangle$, obtained from the measured cross section for $p_{\mathrm{T}} < 8$ GeV/c, which is extrapolated up to $p_{\mathrm{T}} = 26\,\mathrm{GeV}/c$ using FONLL. The ratio of the yields using TPC–TOF and TPC–EMCal analyses in the overlapping interval of $3 < p_{\mathrm{T}} < 8\,\mathrm{GeV}/c$ in Pb-Pb collisions is shown in the bottom panel.

The p_{T} differential yields for electrons from beauty-hadron decays in the 10% most central Pb-Pb collisions are shown in Fig. 4. The yields are obtained using the four-template method with TPC-TOF detectors in the interval $2 < p_{\mathrm{T}} < 8\,\mathrm{GeV}/c$, and using the two-template method with TPC-EMCal detectors in the interval $3 < p_{\mathrm{T}} < 26\,\mathrm{GeV}/c$. The ratio of the yields from the two methods in the overlapping interval of $3 < p_{\mathrm{T}} < 8\,\mathrm{GeV}/c$ is shown in the bottom panel of Fig. 4. The systematic uncertainties are propagated as uncorrelated from all sources, except for the 15% uncertainty assigned for the differences in the results of the two methods, which is not considered in the ratio. Some of the remaining systematic uncertainties have common sources and are thus correlated to some degree, which is difficult to estimate. The ratio is consistent with unity within statistical and systematic uncertainties. For the final yield, TPC–TOF results were used in the overlapping p_{T} range because of their smaller statistical and systematic uncertainties. The Pb-Pb results are shown together with the pp results, scaled by the estimated nuclear overlap function [92], which is proportional to the number of binary collisions.

The nuclear modification factor for electrons from beauty-hadron decays in Pb-Pb collisions as a function of p_{T} in the 0–10% centrality interval is shown in Fig. 5. The nuclear modification factor in the measured p_{T} range of

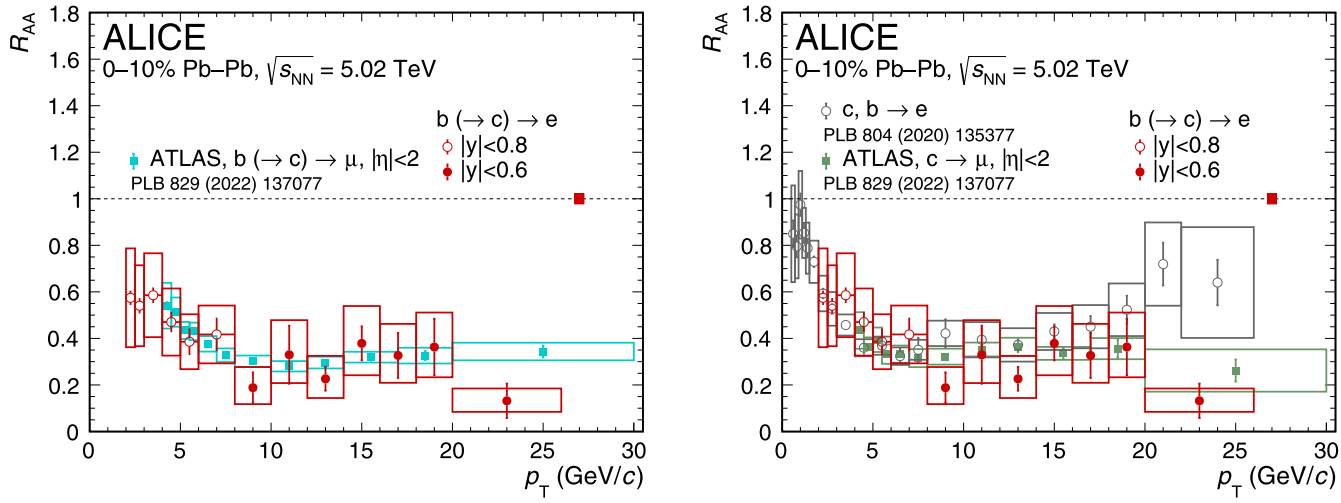

FIG. 5. Nuclear modification factor of electrons from beauty-hadron decays in the 10% most central Pb-Pb collisions at $\sqrt{s_{NN}} = 5.02$ TeV. Left: Comparison with R_{AA} of muons from beauty-hadron decays measured by the ATLAS collaboration [77]. Right: comparison with the measurements of R_{AA} of electrons from heavy-flavor hadron (beauty plus charm) decays [109], and with the R_{AA} of muons from charm-hadron decays measured by the ATLAS collaboration [77].

$2 < p_T < 26$ GeV/c is lower than unity, consistent with the expectation of suppression of the yield in this p_T interval due to in-medium parton energy loss. Considering that the systematic uncertainties are mostly correlated across p_T intervals, the measured R_{AA} suggests a broadly increasing suppression with increasing p_T up to $p_T \approx 5$ GeV/c. For p_T above 8 GeV/c, the R_{AA} does not change significantly with values between 0.2 and 0.4, and a maximum suppression observed for p_T around 8–10 GeV/c. The measured R_{AA} of electrons from beauty-hadron decays is compared with the R_{AA} of muons from beauty-hadron decays, measured by the ATLAS collaboration [77], in the 10% most central Pb-Pb collisions at $\sqrt{s_{NN}} = 5.02$ TeV in the interval $4 < p_T < 30$ GeV/c and $|y| < 2$. As mentioned above, the pp reference for the ATLAS measurement decreases faster with p_T than the central FONLL extrapolation used here. However, the two measurements are consistent with each other within statistical and systematic uncertainties. The nonprompt D^0 meson [69] and the nonprompt D_s^+ meson [71] R_{AA} measured by the ALICE collaboration in the 10% most central Pb-Pb collisions also show a similar p_T dependence, with the minimum value at around 0.35 for $p_T \approx 10$ GeV/c. Possible differences may arise between the R_{AA} of leptons and nonprompt D mesons due to different decay kinematics of B mesons in the two decay channels. For $p_T > 4$ GeV/c, the R_{AA} of electrons from beauty-hadron decays shows a similar suppression as observed in similar measurements at lower collision energies, namely at $\sqrt{s_{NN}} = 2.76$ TeV by the ALICE collaboration [72] at the LHC, and at $\sqrt{s_{NN}} = 0.2$ TeV by the PHENIX [76] and the STAR [75] collaborations at RHIC. Within large uncertainties, the results at lower collision energies show somewhat higher R_{AA} values at lower p_T. The similar R_{AA} values at high p_T could be caused by the the interplay between the medium temperature and density, and the p_T distribution of beauty quarks at the two collision energies [120]. A similar trend was observed for prompt D mesons when comparing results at the two collisions energies [55].

To understand the mass ordering effects on the energy loss, the R_{AA} of electrons from beauty-hadron decays is compared with the R_{AA} of electrons from heavy-flavor hadron (beauty and charm) decays [109], and with the R_{AA} of muons from charm-hadron decays measured by the ATLAS collaboration [77], as a function of p_T in the 10% most central Pb-Pb collisions, in the right panel of Fig. 5. The electrons from heavy-flavor hadron decays originate mostly from charm-hadron decays at low p_T, more than 70% for p_T <4 GeV/c, with the contribution from beauty-hadron decays that increases with increasing p_T [121], and becomes the dominant source (>70%) for p_T >8 GeV/c. Within uncertainties, the R_{AA} of $b(\rightarrow c) \rightarrow e$ in the 10% most central Pb-Pb collisions shows similar values to that of $c \rightarrow \mu$ and $c, b \rightarrow e$. While the central points of the R_{AA} values might be slightly higher for $b(\rightarrow c) \rightarrow e$ compared to $c \rightarrow \mu$ at low p_T (<5 GeV/c), the values are very similar and consistent within the uncertainties, and thus precise measurements of leptons from beauty-hadron decays would be required to see a potential difference.

The nuclear modification factor of electrons from beauty-hadron decays is compared with DREENA-B [122] and DAB-MOD M&T [123] model predictions in the left panel of Fig. 6, and with MC@sHQ [124], PHSD [125], and LIDO [126] models in the right panel of Fig. 6. All models include the assumption of a dynamically expanding QGP. Each model makes different hypotheses about the mass dependence of the energy loss within the QGP, transport dynamics, and hadronization of the beauty quarks. All the models include collisional and radiative energy-loss processes with the exception of PHSD, which only includes collisional energy loss. The models MC@sHQ, PHSD, and LIDO include hadronization via coalescence [127] at low and intermediate momentum, and via fragmentation at high momentum, while the DREENA-B and DAB-MOD M&T models use fragmentation in the full momentum range considered. Initial-state effects are included by using nuclear PDFs in the calculation of the initial p_T distributions of heavy quarks in all models,

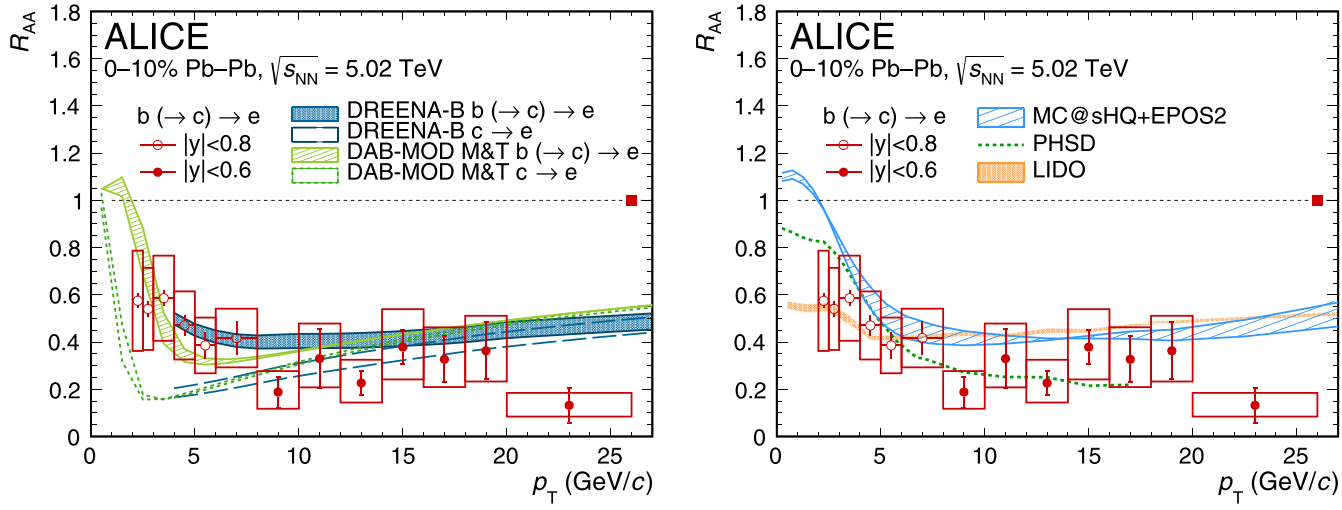

FIG. 6. Nuclear modification factor of electrons from beauty-hadron decays in the 10% most central Pb-Pb collisions at $\sqrt{s_{NN}} = 5.02$ TeV compared with predictions from several theoretical calculations. Left: Comparison with predictions from DREENA-B [122] and DAB-MOD M&T [123] models for electrons from beauty and charm decays. Right: Comparison with predictions from MC@sHQ [124], PHSD [125], and LIDO [126] calculations for electrons from beauty decays.

except for DAB-MOD. All the models give a fair description of the data within the uncertainties of the measurement. For $p_T > 5$ GeV/c, all models except for PHSD predict similar R_{AA}, with values lying on the upper edge of the data uncertainties. The PHSD model gives lower R_{AA} values possibly due to the higher probability of large momentum transfers in the in-medium interactions as compared to the other models [125]. Predictions for all models, but DREENA-B, are available down to very low p_T, where they show significant differences among each other. However, measurements with improved precision will be needed to discriminate among these models. The left panel of Fig. 6 also shows the predictions for $c \to e$ R_{AA} from DREENA-B [122] and DAB-MOD M&T [123] models. The difference in the R_{AA} of electrons from charm- and beauty-hadron decays is larger at low p_T and reduces at high p_T where the mass effects become negligible. However, the current measurements (see right panel of Fig. 5) do not have enough precision to confirm this prediction.

As previously observed with charm measurements [55,58], it is challenging for models to simultaneously describe R_{AA} and v_2 of heavy-flavor particles, allowing data to provide constraints to the model ingredients and parameters to describe the interaction of heavy quarks with the QGP medium. Among the models presented in this article, the MC@sHQ [124] and LIDO [126] models best describe the R_{AA}, v_2, and v_3 measurements of D mesons [55]. In the beauty sector, the v_2 of leptons from beauty-hadron decays was measured by the ALICE [78] and ATLAS [77] collaborations. The ALICE measurement of electrons from beauty-hadron decays was performed in the interval $1.3 < p_T < 6$ GeV/c, and compared with predictions from MC@sHQ [124], PHSD [125], and LIDO [126] models. These models predict similar p_T-dependent v_2 values in the full p_T interval, and all models describe the data within uncertainties above 2 GeV/c. Some parameters of the LIDO model were calibrated to reproduce previous D meson and B meson measurements by the ALICE and CMS collaborations [126]. Extension of v_2 measurements to higher p_T would be beneficial for comparing the models at high p_T. The v_2 of muons from beauty-hadron decays from the ATLAS collaboration [77], measured in the interval $4 < p_T < 20$ GeV/c, was compared with DREENA-B [122] and DAB-MOD M&T [123] models. While the two models provide similar $b \to e$ R_{AA} predictions in the available p_T range, they significantly vary in v_2 predictions below 10 GeV/c, where DREENA-B model is qualitatively in better agreement with the data. In this context, measurements of beauty decay electrons can provide additional and important constraints for modeling the heavy quark in-medium interactions and hadronization.

V. SUMMARY

The p_T-differential production of beauty-hadron decay electrons was measured in pp collisions and in the 10% most central Pb-Pb collisions at $\sqrt{s_{NN}} = 5.02$ TeV. The measurements are based on electron identification together with a fit to the track impact parameter distributions to extract the beauty contribution. The measured p_T-differential cross section in pp collisions lies at the upper edge of the FONLL uncertainty band, and shows some tension with GM-VFNS calculations at low p_T. The measured nuclear modification factor in central Pb-Pb collisions shows an increasing suppression with increasing p_T up to ≈5 GeV/c, and is almost constant at higher p_T. The maximum suppression of about a factor 3 is observed around 8–10 GeV/c. The measured R_{AA} of $b(\to c) \to e$ is consistent with the measurement of $b(\to c) \to \mu$ by the ATLAS collaboration. The R_{AA} of leptons from beauty-hadron decays shows a similar suppression and shape compared to charm-hadron decays within uncertainties. The results are consistent with several transport models implementing interactions of heavy quarks with a QGP formed in Pb-Pb collisions. While models implementing radiative and

collisional energy loss processes predict similar R_{AA} values at high p_{T}, significant differences among models exist at low p_{T}, but more precise measurements are needed to constrain the model parameters further.

ACKNOWLEDGMENTS

The ALICE collaboration thanks all its engineers and technicians for their invaluable contributions to the construction of the experiment and the CERN accelerator teams for the outstanding performance of the LHC complex. The ALICE collaboration gratefully acknowledges the resources and support provided by all Grid centers and the Worldwide LHC Computing Grid (WLCG) collaboration. The ALICE collaboration acknowledges the following funding agencies for their support in building and running the ALICE detector: A. I. Alikhanyan National Science Laboratory (Yerevan Physics Institute) Foundation (ANSL), State Committee of Science and World Federation of Scientists (WFS), Armenia; Austrian Academy of Sciences, Austrian Science Fund (FWF): [M 2467-N36] and Nationalstiftung für Forschung, Technologie und Entwicklung, Austria; Ministry of Communications and High Technologies, National Nuclear Research Center, Azerbaijan; Conselho Nacional de Desenvolvimento Científico e Tecnológico (CNPq), Financiadora de Estudos e Projetos (Finep), Fundação de Amparo à Pesquisa do Estado de São Paulo (FAPESP) and Universidade Federal do Rio Grande do Sul (UFRGS), Brazil; Bulgarian Ministry of Education and Science, within the National Roadmap for Research Infrastructures 2020–2027 (object CERN), Bulgaria; Ministry of Education of China (MOEC), Ministry of Science & Technology of China (MSTC) and National Natural Science Foundation of China (NSFC), China; Ministry of Science and Education and Croatian Science Foundation, Croatia; Centro de Aplicaciones Tecnológicas y Desarrollo Nuclear (CEADEN), Cubaenergía, Cuba; Ministry of Education, Youth and Sports of the Czech Republic, Czech Republic; The Danish Council for Independent Research | Natural Sciences, the VILLUM FONDEN and Danish National Research Foundation (DNRF), Denmark; Helsinki Institute of Physics (HIP), Finland; Commissariat à l'Energie Atomique (CEA) and Institut National de Physique Nucléaire et de Physique des Particules (IN2P3) and Centre National de la Recherche Scientifique (CNRS), France; Bundesministerium für Bildung und Forschung (BMBF) and GSI Helmholtzzentrum für Schwerionenforschung GmbH, Germany; General Secretariat for Research and Technology, Ministry of Education, Research and Religions, Greece; National Research, Development and Innovation Office, Hungary; Department of Atomic Energy Government of India (DAE), Department of Science and Technology, Government of India (DST), University Grants Commission, Government of India (UGC) and Council of Scientific and Industrial Research (CSIR), India; National Research and Innovation Agency–BRIN, Indonesia; Istituto Nazionale di Fisica Nucleare (INFN), Italy; Japanese Ministry of Education, Culture, Sports, Science and Technology (MEXT) and Japan Society for the Promotion of Science (JSPS) KAKENHI, Japan; Consejo Nacional de Ciencia (CONACYT) y Tecnología, through Fondo de Cooperación Internacional en Ciencia y Tecnología (FONCICYT) and Dirección General de Asuntos del Personal Academico (DGAPA), Mexico; Nederlandse Organisatie voor Wetenschappelijk Onderzoek (NWO), Netherlands; The Research Council of Norway, Norway; Commission on Science and Technology for Sustainable Development in the South (COMSATS), Pakistan; Pontificia Universidad Católica del Perú, Peru; Ministry of Education and Science, National Science Centre and WUT ID-UB, Poland; Korea Institute of Science and Technology Information and National Research Foundation of Korea (NRF), Republic of Korea; Ministry of Education and Scientific Research, Institute of Atomic Physics, Ministry of Research and Innovation and Institute of Atomic Physics and University Politehnica of Bucharest, Romania; Ministry of Education, Science, Research and Sport of the Slovak Republic, Slovakia; National Research Foundation of South Africa, South Africa; Swedish Research Council (VR) and Knut & Alice Wallenberg Foundation (KAW), Sweden; European Organization for Nuclear Research, Switzerland; Suranaree University of Technology (SUT), National Science and Technology Development Agency (NSTDA), Thailand Science Research and Innovation (TSRI) and National Science, Research and Innovation Fund (NSRF), Thailand; Turkish Energy, Nuclear and Mineral Research Agency (TENMAK), Turkey; National Academy of Sciences of Ukraine, Ukraine; Science and Technology Facilities Council (STFC), United Kingdom; National Science Foundation of the United States of America (NSF) and United States Department of Energy, Office of Nuclear Physics (DOE NP), United States of America. In addition, individual groups or members have received support from: Marie Skłodowska Curie, European Research Council, Strong 2020 - Horizon 2020 (Grants No. 950692, No. 824093, and No. 896850), European Union; Academy of Finland (Center of Excellence in Quark Matter) (Grants No. 346327 and No. 346328), Finland; Programa de Apoyos para la Superación del Personal Académico, UNAM, Mexico; the DST-DAAD Project-based Personnel Exchange Programme, India.

[1] F. Kheyri, M. Khodadi, and H. R. Sepangi, Horava-Lifshitz early universe phase transition beyond detailed balance, Eur. Phys. J. C **73**, 2286 (2013).

[2] A. Bazavov *et al.*, The chiral and deconfinement aspects of the QCD transition, Phys. Rev. D **85**, 054503 (2012).

[3] S. Borsányi, Z. Fodor, C. Hoelbling, S. D. Katz, S. Krieg, C. Ratti, and K. K. Szabo, Recent results on the equation of state of QCD, PoS **LATTICE2014**, 224 (2015).

[4] A. Bazavov *et al.* (HotQCD Collaboration), Chiral crossover in QCD at zero and nonzero chemical potentials, Phys. Lett. B **795**, 15 (2019).

[5] A. Bazavov *et al.*, Equation of state and QCD transition at finite temperature, Phys. Rev. D **80**, 014504 (2009).

[6] P. Braun-Munzinger, V. Koch, T. Schäfer, and J. Stachel, Properties of hot and dense matter from relativistic heavy ion collisions, Phys. Rep. **621**, 76 (2016).

[7] E. V. Shuryak, Quark-gluon plasma and hadronic production of leptons, photons, and psions, Phys. Lett. B **78**, 150 (1978).

[8] T. Csörgő, New form of matter at CERN SPS: Quark matter but not quark gluon plasma, Nucl. Phys. B Proc. Suppl. **92**, 62 (2001).

[9] D. Teaney, J. Lauret, and E. V. Shuryak, Flow at the SPS and RHIC as a Quark Gluon Plasma Signature, Phys. Rev. Lett. **86**, 4783 (2001).

[10] I. Arsene *et al.* (BRAHMS Collaboration), Quark gluon plasma and color glass condensate at RHIC? The Perspective from the BRAHMS experiment, Nucl. Phys. A **757**, 1 (2005).

[11] B. B. Back *et al.* (PHOBOS Collaboration), The PHOBOS perspective on discoveries at RHIC, Nucl. Phys. A **757**, 28 (2005).

[12] J. Adams *et al.* (STAR Collaboration), Experimental and theoretical challenges in the search for the quark gluon plasma: The STAR Collaboration's critical assessment of the evidence from RHIC collisions, Nucl. Phys. A **757**, 102 (2005).

[13] K. Adcox *et al.* (PHENIX Collaboration), Formation of dense partonic matter in relativistic nucleus-nucleus collisions at RHIC: Experimental evaluation by the PHENIX collaboration, Nucl. Phys. A **757**, 184 (2005).

[14] B. Müller, J. Schukraft, and B. Wyslouch, First Results from Pb+Pb collisions at the LHC, Annu. Rev. Nucl. Part. Sci. **62**, 361 (2012).

[15] ALICE Collaboration, The ALICE experiment—A journey through QCD, arXiv:2211.04384.

[16] A. Andronic, P. Braun-Munzinger, K. Redlich, and J. Stachel, Statistical hadronization of heavy quarks in ultra-relativistic nucleus-nucleus collisions, Nucl. Phys. A **789**, 334 (2007).

[17] A. Andronic *et al.*, Heavy-flavour and quarkonium production in the LHC era: From proton-proton to heavy-ion collisions, Eur. Phys. J. C **76**, 107 (2016).

[18] F.-M. Liu and S.-X. Liu, Quark-gluon plasma formation time and direct photons from heavy ion collisions, Phys. Rev. C **89**, 034906 (2014).

[19] M. Cacciari, M. Greco, and P. Nason, The p_{T} spectrum in heavy flavor hadroproduction, J. High Energy Phys. 05 (1998) 007.

[20] M. Cacciari, S. Frixione, and P. Nason, The p_{T} spectrum in heavy flavor photoproduction, J. High Energy Phys. 03 (2001) 006.

[21] M. Cacciari, S. Frixione, N. Houdeau, M. L. Mangano, P. Nason, and G. Ridolfi, Theoretical predictions for charm and bottom production at the LHC, J. High Energy Phys. 10 (2012) 137.

[22] P. Bolzoni and G. Kramer, Inclusive lepton production from heavy-hadron decay in pp collisions at the LHC, Nucl. Phys. B **872**, 253 (2013); **876**, 334(E) (2013).

[23] S. Cao *et al.*, Toward the determination of heavy-quark transport coefficients in quark-gluon plasma, Phys. Rev. C **99**, 054907 (2019).

[24] R. Baier, D. Schiff, and B. G. Zakharov, Energy loss in perturbative QCD, Ann. Rev. Nucl. Part. Sci. **50**, 37 (2000).

[25] Y. L. Dokshitzer and D. E. Kharzeev, Heavy quark colorimetry of QCD matter, Phys. Lett. B **519**, 199 (2001).

[26] N. Armesto, C. A. Salgado, and U. A. Wiedemann, Medium induced gluon radiation off massive quarks fills the dead cone, Phys. Rev. D **69**, 114003 (2004).

[27] S. Wicks, W. Horowitz, M. Djordjevic, and M. Gyulassy, Heavy quark jet quenching with collisional plus radiative energy loss and path length fluctuations, Nucl. Phys. A **783**, 493 (2007).

[28] B.-W. Zhang, E. Wang, and X.-N. Wang, Heavy Quark Energy Loss in Nuclear Medium, Phys. Rev. Lett. **93**, 072301 (2004).

[29] A. Adil and I. Vitev, Collisional dissociation of heavy mesons in dense QCD matter, Phys. Lett. B **649**, 139 (2007).

[30] B.-W. Zhang, C.-M. Ko, and W. Liu, Thermal charm production in a quark-gluon plasma in Pb-Pb collisions at $\sqrt{s_{NN}} =$ 5.5 TeV, Phys. Rev. C **77**, 024901 (2008).

[31] P. Braun-Munzinger, Quarkonium production in ultra-relativistic nuclear collisions: Suppression versus enhancement, J. Phys. G: Nucl. Part. Phys. **34**, S471 (2007).

[32] M. Djordjevic, M. Gyulassy, and S. Wicks, Open Charm and Beauty at Ultrarelativistic Heavy Ion Colliders, Phys. Rev. Lett. **94**, 112301 (2005).

[33] S. Acharya *et al.* (ALICE Collaboration), Direct observation of the dead-cone effect in quantum chromodynamics, Nature (London) **605**, 440 (2022).

[34] C. Loizides, J. Kamin, and D. d'Enterria, Improved Monte Carlo Glauber predictions at present and future nuclear colliders, Phys. Rev. C **97**, 054910 (2018); **99**, 019901(E) (2019).

[35] D. d'Enterria and C. Loizides, Progress in the Glauber model at collider energies, Annu. Rev. Nucl. Part. Sci. **71**, 315 (2021).

[36] M. M. Aggarwal *et al.* (STAR Collaboration), Measurement of the Bottom Contribution to Nonphotonic Electron Production in $p + p$ Collisions at $\sqrt{s} = 200$ GeV, Phys. Rev. Lett. **105**, 202301 (2010).

[37] A. Adare *et al.* (PHENIX Collaboration), Measurement of Bottom Versus Charm as a Function of Transverse Momentum with Electron-Hadron Correlations in $p + p$ Collisions at $\sqrt{s} = 200$ GeV, Phys. Rev. Lett. **103**, 082002 (2009).

[38] D. Acosta *et al.* (CDF Collaboration), Measurement of the J/ψ meson and B-hadron production cross sections in $p\bar{p}$ collisions at $\sqrt{s} = 1960$ GeV, Phys. Rev. D **71**, 032001 (2005).

[39] B. Abelev *et al.* (ALICE Collaboration), Measurement of electrons from beauty hadron decays in pp collisions at $\sqrt{s} = 7$ TeV, Phys. Lett. B **721**, 13 (2013); **763**, 507(E) (2016).

[40] B. Abelev *et al.* (ALICE Collaboration), Measurement of electrons from semileptonic heavy-flavor hadron decays in pp collisions at $\sqrt{s} = 2.76$ TeV, Phys. Rev. D **91**, 012001 (2015).

[41] R. Aaij *et al.* (LHCb Collaboration), Measurement of the $B^{\pm}$ production cross-section in pp collisions at $\sqrt{s} = 7$ TeV, J. High Energy Phys. 04 (2012) 093.

[42] G. Aad *et al.* (ATLAS Collaboration), Measurement of the differential cross-sections of inclusive, prompt and nonprompt J/ψ production in proton-proton collisions at $\sqrt{s} = 7$ TeV, Nucl. Phys. B **850**, 387 (2011).

[43] B. Abelev *et al.* (ALICE Collaboration), Measurement of prompt J/ψ and beauty hadron production cross sections at mid-rapidity in pp collisions at $\sqrt{s} = 7$ TeV, J. High Energy Phys. 11 (2012) 065.

[44] G. Aad *et al.* (ATLAS Collaboration), Measurement of the B-hadron production cross section using decays to $D^*\mu^- X$ final states in pp collisions at $\sqrt{s} = 7$ TeV with the ATLAS detector, Nucl. Phys. B **864**, 341 (2012).

[45] G. Aad *et al.* (ATLAS Collaboration), Measurement of the differential cross-section of B^+ meson production in pp collisions at $\sqrt{s} = 7$ TeV at ATLAS, J. High Energy Phys. 10 (2013) 042.

[46] S. Chatrchyan *et al.* (CMS Collaboration), Measurement of the cross section for production of $b\bar{b}X$ decaying to muons in pp collisions at $\sqrt{s} = 7$ TeV, J. High Energy Phys. 06 (2012) 110.

[47] V. Khachatryan *et al.* (CMS Collaboration), Prompt and non-prompt J/ψ production in pp collisions at $\sqrt{s} = 7$ TeV, Eur. Phys. J. C **71**, 1575 (2011).

[48] V. Khachatryan *et al.* (CMS Collaboration), Measurement of the B^+ Production Cross Section in pp Collisions at $\sqrt{s} =$ 7 TeV, Phys. Rev. Lett. **106**, 112001 (2011).

[49] S. Chatrchyan *et al.* (CMS Collaboration), Measurement of the B^0 Production Cross Section in pp Collisions at $\sqrt{s} = 7$ TeV, Phys. Rev. Lett. **106**, 252001 (2011).

[50] S. Chatrchyan *et al.* (CMS Collaboration), Measurement of the B_s^0 production cross section with $B_s^0 \to J/\psi\phi$ decays in pp collisions at $\sqrt{s}$=7TeV, Phys. Rev. D **84**, 052008 (2011).

[51] V. Khachatryan *et al.* (CMS Collaboration), Measurement of the total and differential inclusive B^+ hadron cross sections in pp collisions at $\sqrt{s} = 13$ TeV, Phys. Lett. B **771**, 435 (2017).

[52] S. Acharya *et al.* (ALICE Collaboration), Measurement of beauty and charm production in pp collisions at $\sqrt{s} =$ 5.02 TeV via nonprompt and prompt D mesons, J. High Energy Phys. 05 (2021) 220.

[53] S. Acharya *et al.* (ALICE Collaboration), Prompt and non-prompt J/ψ production cross sections at midrapidity in proton-proton collisions at $\sqrt{s} = 5.02$ and 13 TeV, J. High Energy Phys. 03 (2022) 190.

[54] S. Acharya *et al.* (ALICE Collaboration), Dielectron and heavy-quark production in inelastic and high-multiplicity proton-proton collisions at $\sqrt{s_{NN}} = 13$ TeV, Phys. Lett. B **788**, 505 (2019).

[55] S. Acharya *et al.* (ALICE Collaboration), Prompt D^0, D^+, and D^{*+} production in Pb-Pb collisions at $\sqrt{s_{NN}} = 5.02$ TeV, J. High Energy Phys. 01 (2022) 174.

[56] A. M. Sirunyan *et al.* (CMS Collaboration), Nuclear modification factor of D^0 mesons in Pb-Pb collisions at $\sqrt{s_{NN}} =$ 5.02 TeV, Phys. Lett. B **782**, 474 (2018).

[57] S. Acharya *et al.* (ALICE Collaboration), Measurement of prompt D_s^+-meson production and azimuthal anisotropy in Pb-Pb collisions at $\sqrt{s_{NN}} = 5.02$ TeV, Phys. Lett. B **827**, 136986 (2022).

[58] S. Acharya *et al.* (ALICE Collaboration), D-Meson Azimuthal Anisotropy in Midcentral Pb-Pb Collisions at $\sqrt{s_{NN}} =$ 5.02 TeV, Phys. Rev. Lett. **120**, 102301 (2018).

[59] S. Acharya *et al.* (ALICE Collaboration), Transverse-momentum and event-shape dependence of D meson flow harmonics in Pb-Pb collisions at $\sqrt{s_{NN}} = 5.02$ TeV, Phys. Lett. B **813**, 136054 (2021).

[60] A. Adare *et al.* (PHENIX Collaboration), Heavy quark production in $p + p$ and energy loss and flow of heavy quarks in Au+Au collisions at $\sqrt{s_{NN}} = 200$ GeV, Phys. Rev. C **84**, 044905 (2011).

[61] L. Adamczyk *et al.* (STAR Collaboration), Elliptic flow of electrons from heavy-flavor hadron decays in Au + Au collisions at $\sqrt{s_{NN}} = 200$, 62.4, and 39 GeV, Phys. Rev. C **95**, 034907 (2017).

[62] L. Adamczyk *et al.* (STAR Collaboration), Measurement of D^0 Azimuthal Anisotropy at Midrapidity in Au+Au Collisions at $\sqrt{s_{NN}}$=200 GeV, Phys. Rev. Lett. **118**, 212301 (2017).

[63] A. Beraudo *et al.*, Extraction of heavy-flavor transport coefficients in QCD matter, Nucl. Phys. A **979**, 21 (2018).

[64] A. M. Sirunyan *et al.* (CMS Collaboration), Measurement of the $B^{\pm}$ Meson Nuclear Modification Factor in Pb-Pb Collisions at $\sqrt{s_{NN}} = 5.02$ TeV, Phys. Rev. Lett. **119**, 152301 (2017).

[65] M. Aaboud *et al.* (ATLAS Collaboration), Measurement of the relative $B_c^{\pm}/B^{\pm}$ production cross section with the ATLAS detector at $\sqrt{s} = 8$ TeV, Phys. Rev. D **104**, 012010 (2021).

[66] P. Zyla *et al.* (Particle Data Group Collaboration), Review of particle physics, PTEP **2020**, 083C01 (2020).

[67] M. Aaboud *et al.* (ATLAS Collaboration), Prompt and nonprompt J/ψ and $\psi(2S)$ suppression at high transverse momentum in 5.02TeV Pb+Pb collisions with the ATLAS experiment, Eur. Phys. J. C **78**, 762 (2018).

[68] A. M. Sirunyan *et al.* (CMS Collaboration), Measurement of prompt and nonprompt charmonium suppression in PbPb collisions at 5.02 TeV, Eur. Phys. J. C **78**, 509 (2018).

[69] S. Acharya *et al.* (ALICE Collaboration), Measurement of beauty production via nonprompt D^0 mesons in Pb-Pb collisions at $\sqrt{s_{NN}} = 5.02$ TeV, J. High Energy Phys. 12 (2022) 126.

[70] A. M. Sirunyan *et al.* (CMS Collaboration), Studies of Beauty Suppression Via Nonprompt D^0 Mesons in Pb-Pb Collisions at $Q^2 = 4\text{GeV}^2$, Phys. Rev. Lett. **123**, 022001 (2019).

[71] ALICE Collaboration, Measurement of beauty-strange meson production in $\text{Pb} - \text{Pb}$ collisions at $\sqrt{s_{NN}} = 5.02$ TeV via nonprompt D_s^+ mesons, arXiv:2204.10386.

[72] J. Adam *et al.* (ALICE Collaboration), Measurement of electrons from beauty-hadron decays in p-Pb collisions at $\sqrt{s_{NN}} =$ 5.02 TeV and Pb-Pb collisions at $\sqrt{s_{NN}} = 2.76$ TeV, J. High Energy Phys. 07 (2017) 052.

[73] A. Adare *et al.* (PHENIX Collaboration), Single electron yields from semileptonic charm and bottom hadron decays in Au+Au collisions at $\sqrt{s_{NN}} = 200$ GeV, Phys. Rev. C **93**, 034904 (2016).

[74] S. Acharya *et al.* (ALICE Collaboration), Production of muons from heavy-flavor hadron decays at high transverse momentum in Pb-Pb collisions at $\sqrt{s_{NN}} = 5.02$ and 2.76 TeV, Phys. Lett. B **820**, 136558 (2021).

[75] M. S. Abdallah *et al.* (STAR Collaboration), Evidence of mass ordering of charm and bottom quark energy loss in Au+Au collisions at RHIC, Eur. Phys. J. C **82**, 1150 (2022); **83**, 455(E) (2023).

[76] U. A. Acharya *et al.* (PHENIX Collaboration), Charm- and bottom-quark production in Au+Au collisions at $\sqrt{s_{NN}} =$ 200 GeV, arXiv:2203.17058.

[77] G. Aad *et al.* (ATLAS Collaboration), Measurement of the nuclear modification factor for muons from charm and bottom hadrons in Pb+Pb collisions at 5.02 TeV with the ATLAS detector, Phys. Lett. B **829**, 137077 (2022).

[78] S. Acharya *et al.* (ALICE Collaboration), Elliptic Flow of Electrons from Beauty-Hadron Decays in Pb-Pb Collisions at $\sqrt{s_{NN}} = 5.02$ TeV, Phys. Rev. Lett. **126**, 162001 (2021).

[79] G. Aad *et al.* (ATLAS Collaboration), Measurement of azimuthal anisotropy of muons from charm and bottom hadrons in Pb+Pb collisions at $\sqrt{s_{NN}} = 5.02$ TeV with the ATLAS detector, Phys. Lett. B **807**, 135595 (2020).

[80] K. Aamodt *et al.* (ALICE Collaboration), The ALICE experiment at the CERN LHC, JINST **3**, S08002 (2008).

[81] B. Abelev *et al.* (ALICE Collaboration), Performance of the ALICE Experiment at the CERN LHC, Int. J. Mod. Phys. A **29**, 1430044 (2014).

[82] K. Aamodt *et al.* (ALICE Collaboration), Alignment of the ALICE inner tracking system with cosmic-ray tracks, JINST **5**, P03003 (2010).

[83] J. Alme *et al.*, The ALICE TPC, a large 3-dimensional tracking device with fast readout for ultra-high multiplicity events, Nucl. Instrum. Methods Phys. Res., Sect. A **622**, 316 (2010).

[84] A. Akindinov *et al.*, The commissioning of the ALICE time-of-flight detector and results from the 2008 cosmic-ray data taking, Nucl. Instrum. Methods Phys. Res., Sect. A **615**, 37 (2010).

[85] P. Cortese *et al.* (ALICE Collaboration), ALICE Electromagnetic Calorimeter Technical Design Report, Tech. Rep. CERN-LHCC-2008-014. ALICE-TDR-14 (Aug. 2008), http://cds.cern.ch/record/1121574.

[86] J. Adam *et al.* (ALICE Collaboration), Determination of the event collision time with the ALICE detector at the LHC, Eur. Phys. J. Plus **132**, 99 (2017).

[87] S. Acharya *et al.* (ALICE Collaboration), Performance of the ALICE Electromagnetic Calorimeter, **JINST**, **18**, P08007 (2023.

[88] G. S. Atoian *et al.*, Lead scintillator electromagnetic calorimeter with wavelength shifting fiber readout, Nucl. Instrum. Methods Phys. Res., Sect. A **320**, 144 (1992).

[89] E. Abbas *et al.* (ALICE Collaboration), Performance of the ALICE VZERO system, J. Inst. **8**, P10016 (2013).

[90] ALICE Collaboration, ALICE luminosity determination for Pb-Pb collisions at $\sqrt{s_{NN}} = 5.02$ TeV, arXiv:2204.10148.

[91] P. Cortese (ALICE Collaboration), Performance of the ALICE zero degree calorimeters and upgrade strategy, J. Phys.: Conf. Ser. **1162**, 012006 (2019).

[92] ALICE Collaboration, Centrality determination in heavy ion collisions, ALICE-PUBLIC-2018-011 (Aug. 2018), http://cds.cern.ch/record/2636623.

[93] B. Abelev *et al.* (ALICE Collaboration), Centrality determination of Pb-Pb collisions at $\sqrt{s_{NN}} = 2.76$ TeV with ALICE, Phys. Rev. C **88**, 044909 (2013).

[94] ALICE Collaboration, ALICE 2017 luminosity determination for *pp* collisions at $\sqrt{s} = 5$ TeV, ALICE-PUBLIC-2018-014 (Nov. 2018), http://cds.cern.ch/record/2648933.

[95] B. Abelev *et al.* (ALICE Collaboration), Measurement of electrons from semileptonic heavy-flavour hadron decays in *pp* collisions at $\sqrt{s} = 7$ TeV, Phys. Rev. D **86**, 112007 (2012).

[96] M. Tanabashi *et al.* (Particle Data Group Collaboration), Review of particle physics, Phys. Rev. D **98**, 030001 (2018).

[97] S. Acharya *et al.* (ALICE Collaboration), Production of light-flavor hadrons in *pp* collisions at $\sqrt{s} = 7$ and $\sqrt{s} = 13$ TeV, Eur. Phys. J. C **81**, 256 (2021).

[98] T. C. Awes, F. E. Obenshain, F. Plasil, S. Saini, S. P. Sorensen, and G. R. Young, A Simple method of shower localization and identification in laterally segmented calorimeters, Nucl. Instrum. Methods Phys. Res., Sect. A **311**, 130 (1992).

[99] S. Acharya *et al.* (ALICE Collaboration), Production of π^0 and η mesons up to high transverse momentum in *pp* collisions at 2.76 TeV, Eur. Phys. J. C **77**, 339 (2017).

[100] C. W. Fabjan *et al.* (ALICE Collaboration), ALICE: Physics performance report, J. Phys. G: Nucl. Part. Phys. **32**, 1295 (2006).

[101] T. Sjöstrand, S. Mrenna, and P. Z. Skands, PYTHIA 6.4 physics and manual, J. High Energy Phys. 05 (2006) 026.

[102] X.-N. Wang and M. Gyulassy, HIJING: A Monte Carlo model for multiple jet production in *pp*, *pA*, and *AA* collisions, Phys. Rev. D **44**, 3501 (1991).

[103] R. Brun, F. Bruyant, M. Maire, A. C. McPherson, and P. Zanarini, *GEANT 3: User's Guide Geant 3.10, Geant 3.11; rev. version* (CERN, Geneva, 1987), https://cds.cern.ch/record/1119728.

[104] R. Barlow and C. Beeston, Fitting using finite Monte Carlo samples, Comput. Phys. Commun. **77**, 219 (1993).

[105] S. Acharya *et al.* (ALICE Collaboration), Λ_c^+ production in Pb-Pb collisions at $\sqrt{s_{NN}} = 5.02$ TeV, Phys. Lett. B **793**, 212 (2019).

[106] S. Acharya *et al.* (ALICE Collaboration), Constraining hadronization mechanisms with Λ_c^+/D^0 production ratios in Pb-Pb collisions at $\sqrt{s_{\mathrm{NN}}} = 5.02$ TeV, Phys. Lett. B **839**, 137796 (2023).

[107] S. Acharya *et al.* (ALICE Collaboration), Measurement of D^0, D^+, D^{*+}, and D_s^+ production in Pb-Pb collisions at $\sqrt{s_{NN}} =$ 5.02 TeV, J. High Energy Phys. 10 (2018) 174.

[108] M. He, R. J. Fries, and R. Rapp, Heavy flavor at the large hadron collider in a strong coupling approach, Phys. Lett. B **735**, 445 (2014).

[109] S. Acharya *et al.* (ALICE Collaboration), Measurement of electrons from semileptonic heavy-flavour hadron decays at midrapidity in *pp* and Pb-Pb collisions at $\sqrt{s_{NN}} = 5.02$ TeV, Phys. Lett. B **804**, 135377 (2020).

[110] J. Adam *et al.* (ALICE Collaboration), Measurement of electrons from heavy-flavor hadron decays in *p*-Pb collisions at $\sqrt{s_{\mathrm{NN}}} = 5.02$ TeV, Phys. Lett. B **754**, 81 (2016).

[111] J. Adam *et al.* (ALICE Collaboration), Measurement of the production of high-p_{T} electrons from heavy-flavour hadron decays in Pb-Pb collisions at $\sqrt{s_{NN}} = 2.76$ TeV, Phys. Lett. B **771**, 467 (2017).

[112] S. Acharya *et al.* (ALICE Collaboration), Measurements of low-p_{T} electrons from semileptonic heavy-flavour hadron decays at mid-rapidity in *pp* and Pb-Pb collisions at $\sqrt{s_{NN}} = 2.76$ TeV, J. High Energy Phys. 10 (2018) 061.

[113] F. James, *Statistical Methods in Experimental Physics*, 2nd ed. (World Scientific, Singapore, 2006).

[114] E. Fermi, An attempt of a theory of beta radiation, Z. Phys. **88**, 161 (1934).

[115] F. L. Wilson, Fermi's theory of beta decay, Am. J. Phys. **36**, 1150 (1968).

[116] S. Acharya *et al.* (ALICE Collaboration), Production of charged pions, kaons, and (anti)protons in Pb-Pb and inelastic *pp* collisions at $\sqrt{s_{NN}} = 5.02$ TeV, Phys. Rev. C **101**, 044907 (2020).

[117] R. Aaij *et al.* (LHCb Collaboration), Measurement of *B*-hadron fractions in 13 TeV *pp* collisions, Phys. Rev. D **100**, 031102 (2019).

[118] B. Aubert *et al.* (BaBar Collaboration), Measurement of the electron energy spectrum and its moments in inclusive $B \to X e \nu$ decays, Phys. Rev. D **69**, 111104 (2004).

[119] B. A. Kniehl, G. Kramer, I. Schienbein, and H. Spiesberger, Inclusive B-meson production at the LHC in the GM-VFN scheme, Phys. Rev. D **84**, 094026 (2011).

[120] M. Djordjevic and M. Djordjevic, Predictions of heavy-flavor suppression at 5.1 TeV Pb + Pb collisions at the CERN Large Hadron Collider, Phys. Rev. C **92**, 024918 (2015).

[121] B. Abelev *et al.* (ALICE Collaboration), Beauty production in pp collisions at $\sqrt{s} = 2.76$ TeV measured via semi-electronic decays, Phys. Lett. B **738**, 97 (2014).

[122] D. Zigic, I. Salom, J. Auvinen, M. Djordjevic, and M. Djordjevic, DREENA-B framework: first predictions of R_{AA} and v_2 within dynamical energy loss formalism in evolving QCD medium, Phys. Lett. B **791**, 236 (2019).

[123] C. A. G. Prado, J. Noronha-Hostler, R. Katz, A. A. P. Suaide, J. Noronha, and M. G. Munhoz, Event-by-event correlations between soft hadrons and D^0 mesons in 5.02 TeV PbPb collisions at the CERN Large Hadron Collider, Phys. Rev. C **96**, 064903 (2017).

[124] M. Nahrgang, J. Aichelin, P. B. Gossiaux, and K. Werner, Influence of hadronic bound states above T_c on heavy-quark observables in Pb + Pb collisions at at the CERN Large Hadron Collider, Phys. Rev. C **89**, 014905 (2014).

[125] T. Song, H. Berrehrah, D. Cabrera, J. M. Torres-Rincon, L. Tolos, W. Cassing, and E. Bratkovskaya, Tomography of the quark-gluon-plasma by charm quarks, Phys. Rev. C **92**, 014910 (2015).

[126] W. Ke, Y. Xu, and S. A. Bass, Linearized Boltzmann-Langevin model for heavy quark transport in hot and dense QCD matter, Phys. Rev. C **98**, 064901 (2018).

[127] F. Prino and R. Rapp, Open heavy flavor in QCD matter and in nuclear collisions, J. Phys. G: Nucl. Part. Phys. **43**, 093002 (2016).

S. Acharya,[125] D. Adamová,[86] A. Adler,[69] G. Aglieri Rinella,[32] M. Agnello,[29] N. Agrawal,[50] Z. Ahammed,[132] S. Ahmad,[15] S. U. Ahn,[70] I. Ahuja,[37] A. Akindinov,[140] M. Al-Turany,[97] D. Aleksandrov,[140] B. Alessandro,[55] H. M. Alfanda,[6] R. Alfaro Molina,[66] B. Ali,[15] A. Alici,[25] N. Alizadehvandchali,[114] A. Alkin,[32] J. Alme,[20] G. Alocco,[51] T. Alt,[63] I. Altsybeev,[140] M. N. Anaam,[6] C. Andrei,[45] A. Andronic,[135] V. Anguelov,[94] F. Antinori,[53] P. Antonioli,[50] N. Apadula,[74] L. Aphecetche,[103] H. Appelshäuser,[63] C. Arata,[73] S. Arcelli,[25] M. Aresti,[51] R. Arnaldi,[55] I. C. Arsene,[19] M. Arslandok,[137] A. Augustinus,[32] R. Averbeck,[97] M. D. Azmi,[15] A. Badalà,[52] J. Bae,[104] Y. W. Baek,[40] X. Bai,[118] R. Bailhache,[63] Y. Bailung,[47] A. Balbino,[29] A. Baldisseri,[128] B. Balis,[2] D. Banerjee,[4] Z. Banoo,[91] R. Barbera,[26] F. Barile,[31] L. Barioglio,[95] M. Barlou,[78] G. G. Barnaföldi,[136] L. S. Barnby,[85] V. Barret,[125] L. Barreto,[110] C. Bartels,[117] K. Barth,[32] E. Bartsch,[63] F. Baruffaldi,[27] N. Bastid,[125] S. Basu,[75] G. Batigne,[103] D. Battistini,[95] B. Batyunya,[141] D. Bauri,[46] J. L. Bazo Alba,[101] I. G. Bearden,[83] C. Beattie,[137] P. Becht,[97] D. Behera,[47] I. Belikov,[127] A. D. C. Bell Hechavarria,[135] F. Bellini,[25] R. Bellwied,[114] S. Belokurova,[140] V. Belyaev,[140] G. Bencedi,[136] S. Beole,[24] A. Bercuci,[45] Y. Berdnikov,[140] A. Berdnikova,[94] L. Bergmann,[94] M. G. Besoiu,[62] L. Betev,[32] P. P. Bhaduri,[132] A. Bhasin,[91] M. A. Bhat,[4] B. Bhattacharjee,[41] L. Bianchi,[24] N. Bianchi,[48] J. Bielčík,[35] J. Bielčíková,[86] J. Biernat,[107] A. P. Bigot,[127] A. Bilandzic,[95] G. Biro,[136] S. Biswas,[4] N. Bize,[103] J. T. Blair,[108] D. Blau,[140] M. B. Blidaru,[97] N. Bluhme,[38] C. Blume,[63] G. Boca,[21,54] F. Bock,[87] T. Bodova,[20] A. Bogdanov,[140] S. Boi,[22] J. Bok,[57] L. Boldizsár,[136] A. Bolozdynya,[140] M. Bombara,[37] P. M. Bond,[32] G. Bonomi,[131,54] H. Borel,[128] A. Borissov,[140] A. G. Borquez Carcamo,[94] H. Bossi,[137] E. Botta,[24] Y. E. M. Bouziani,[63] L. Bratrud,[63] P. Braun-Munzinger,[97] M. Bregant,[110] M. Broz,[35] G. E. Bruno,[96,31] D. Budnikov,[140] H. Buesching,[63] S. Bufalino,[29] O. Bugnon,[103] P. Buhler,[102] Z. Buthelezi,[67,121] S. A. Bysiak,[107] M. Cai,[6] H. Caines,[137] A. Caliva,[97] E. Calvo Villar,[101] J. M. M. Camacho,[109] P. Camerini,[23] F. D. M. Canedo,[110] M. Carabas,[124] A. A. Carballo,[32] F. Carnesecchi,[32] R. Caron,[126] J. Castillo Castellanos,[128] F. Catalano,[24,29] C. Ceballos Sanchez,[141] I. Chakaberia,[74] P. Chakraborty,[46] S. Chandra,[132] S. Chapeland,[32] M. Chartier,[117] S. Chattopadhyay,[132] S. Chattopadhyay,[99] T. G. Chavez,[44] T. Cheng,[97,6] C. Cheshkov,[126] B. Cheynis,[126] V. Chibante Barroso,[32] D. D. Chinellato,[111] E. S. Chizzali,[95,*] J. Cho,[57] S. Cho,[57] P. Chochula,[32] P. Christakoglou,[84] C. H. Christensen,[83] P. Christiansen,[75] T. Chujo,[123] M. Ciacco,[29] C. Cicalo,[51] F. Cindolo,[50] M. R. Ciupek,[97] G. Clai,[50,†] F. Colamaria,[49] J. S. Colburn,[100] D. Colella,[96,31] M. Colocci,[32] M. Concas,[55,‡] G. Conesa Balbastre,[73] Z. Conesa del Valle,[72] G. Contin,[23] J. G. Contreras,[35] M. L. Coquet,[128] T. M. Cormier,[87,§] P. Cortese,[130,55] M. R. Cosentino,[112] F. Costa,[32] S. Costanza,[21,54] J. Crkovská,[94] P. Crochet,[125] R. Cruz-Torres,[74] E. Cuautle,[64] P. Cui,[6] A. Dainese,[53] M. C. Danisch,[94] A. Danu,[62] P. Das,[80] P. Das,[4] S. Das,[4] A. R. Dash,[135] S. Dash,[46] A. De Caro,[28] G. de Cataldo,[49] J. de Cuveland,[38] A. De Falco,[22] D. De Gruttola,[28] N. De Marco,[55] C. De Martin,[23] S. De Pasquale,[28] S. Deb,[47] R. J. Debski,[2] K. R. Deja,[133] R. Del Grande,[95] L. Dello Stritto,[28] W. Deng,[6] P. Dhankher,[18] D. Di Bari,[31] A. Di Mauro,[32] R. A. Diaz,[141,7] T. Dietel,[113] Y. Ding,[126,6] R. Divià,[32] D. U. Dixit,[18] Ø. Djuvsland,[20] U. Dmitrieva,[140] A. Dobrin,[62] B. Dönigus,[63] J. M. Dubinski,[133] A. Dubla,[97] S. Dudi,[90] P. Dupieux,[125] M. Durkac,[106] N. Dzalaiova,[12] T. M. Eder,[135] R. J. Ehlers,[87] V. N. Eikeland,[20] F. Eisenhut,[63] D. Elia,[49] B. Erazmus,[103] F. Ercolessi,[25] F. Erhardt,[89] M. R. Ersdal,[20] B. Espagnon,[72] G. Eulisse,[32] D. Evans,[100] S. Evdokimov,[140] L. Fabbietti,[95] M. Faggin,[27] J. Faivre,[73] F. Fan,[6] W. Fan,[74] A. Fantoni,[48] M. Fasel,[87] P. Fecchio,[29] A. Feliciello,[55] G. Feofilov,[140] A. Fernández Téllez,[44] L. Ferrandi,[110] M. B. Ferrer,[32] A. Ferrero,[128] C. Ferrero,[55] A. Ferretti,[24] V. J. G. Feuillard,[94] V. Filova,[35] D. Finogeev,[140] F. M. Fionda,[51] F. Flor,[114] A. N. Flores,[108] S. Foertsch,[67] I. Fokin,[94] S. Fokin,[140] E. Fragiacomo,[56] E. Frajna,[136] U. Fuchs,[32] N. Funicello,[28] C. Furget,[73] A. Furs,[140] T. Fusayasu,[98] J. J. Gaardhøje,[83] M. Gagliardi,[24] A. M. Gago,[101] C. D. Galvan,[109] D. R. Gangadharan,[114] P. Ganoti,[78] C. Garabatos,[97] J. R. A. Garcia,[44] E. Garcia-Solis,[9]

K. Garg,[103] C. Gargiulo,[32] A. Garibli,[81] K. Garner,[135] P. Gasik,[97] E. F. Gauger,[108] A. Gautam,[116] M. B. Gay Ducati,[65] M. Germain,[103] C. Ghosh,[132] M. Giacalone,[25] P. Giubellino,[97,55] P. Giubilato,[27] A. M. C. Glaenzer,[128] P. Glässel,[94] E. Glimos,[120] D. J. Q. Goh,[76] V. Gonzalez,[134] L. H. González-Trueba,[66] M. Gorgon,[2] S. Gotovac,[33] V. Grabski,[66] L. K. Graczykowski,[133] E. Grecka,[86] A. Grelli,[58] C. Grigoras,[32] V. Grigoriev,[140] S. Grigoryan,[141,1] F. Grosa,[32] J. F. Grosse-Oetringhaus,[32] R. Grosso,[97] D. Grund,[35] G. G. Guardiano,[111] R. Guernane,[73] M. Guilbaud,[103] K. Gulbrandsen,[83] T. Gundem,[63] T. Gunji,[122] W. Guo,[6] A. Gupta,[91] R. Gupta,[91] S. P. Guzman,[44] L. Gyulai,[136] M. K. Habib,[97] C. Hadjidakis,[72] F. U. Haider,[91] H. Hamagaki,[76] A. Hamdi,[74] M. Hamid,[6] Y. Han,[138] R. Hannigan,[108] M. R. Haque,[133] J. W. Harris,[137] A. Harton,[9] H. Hassan,[87] D. Hatzifotiadou,[50] P. Hauer,[42] L. B. Havener,[137] S. T. Heckel,[95] E. Hellbär,[97] H. Helstrup,[34] M. Hemmer,[63] T. Herman,[35] G. Herrera Corral,[8] F. Herrmann,[135] S. Herrmann,[126] K. F. Hetland,[34] B. Heybeck,[63] H. Hillemanns,[32] C. Hills,[117] B. Hippolyte,[127] B. Hofman,[58] B. Hohlweger,[84] G. H. Hong,[138] M. Horst,[95] A. Horzyk,[2] R. Hosokawa,[14] Y. Hou,[6] P. Hristov,[32] C. Hughes,[120] P. Huhn,[63] L. M. Huhta,[115] C. V. Hulse,[72] T. J. Humanic,[88] A. Hutson,[114] D. Hutter,[38] J. P. Iddon,[117] R. Ilkaev,[140] H. Ilyas,[13] M. Inaba,[123] G. M. Innocenti,[32] M. Ippolitov,[140] A. Isakov,[86] T. Isidori,[116] M. S. Islam,[99] M. Ivanov,[12] M. Ivanov,[97] V. Ivanov,[140] M. Jablonski,[2] B. Jacak,[74] N. Jacazio,[32] P. M. Jacobs,[74] S. Jadlovska,[106] J. Jadlovsky,[106] S. Jaelani,[82] L. Jaffe,[38] C. Jahnke,[111] M. J. Jakubowska,[133] M. A. Janik,[133] T. Janson,[69] M. Jercic,[89] S. Jia,[10] A. A. P. Jimenez,[64] F. Jonas,[87] J. M. Jowett,[32,97] J. Jung,[63] M. Jung,[63] A. Junique,[32] A. Jusko,[100] M. J. Kabus,[32,133] J. Kaewjai,[105] P. Kalinak,[59] A. S. Kalteyer,[97] A. Kalweit,[32] V. Kaplin,[140] A. Karasu Uysal,[71] D. Karatovic,[89] O. Karavichev,[140] T. Karavicheva,[140] P. Karczmarczyk,[133] E. Karpechev,[140] U. Kebschull,[69] R. Keidel,[139] D. L. D. Keijdener,[58] M. Keil,[32] B. Ketzer,[42] A. M. Khan,[6] S. Khan,[15] A. Khanzadeev,[140] Y. Kharlov,[140] A. Khatun,[116,15] A. Khuntia,[107] M. B. Kidson,[113] B. Kileng,[34] B. Kim,[16] C. Kim,[16] D. J. Kim,[115] E. J. Kim,[68] J. Kim,[138] J. S. Kim,[40] J. Kim,[94] J. Kim,[68] M. Kim,[18,94] S. Kim,[17] T. Kim,[138] K. Kimura,[92] S. Kirsch,[63] I. Kisel,[38] S. Kiselev,[140] A. Kisiel,[133] J. P. Kitowski,[2] J. L. Klay,[5] J. Klein,[32] S. Klein,[74] C. Klein-Bösing,[135] M. Kleiner,[63] T. Klemenz,[95] A. Kluge,[32] A. G. Knospe,[114] C. Kobdaj,[105] T. Kollegger,[97] A. Kondratyev,[141] E. Kondratyuk,[140] J. Konig,[63] S. A. Konigstorfer,[95] P. J. Konopka,[32] G. Kornakov,[133] S. D. Koryciak,[2] A. Kotliarov,[86] V. Kovalenko,[140] M. Kowalski,[107] V. Kozhuharov,[36] I. Králik,[59] A. Kravčáková,[37] L. Kreis,[97] M. Krivda,[100,59] F. Krizek,[86] K. Krizkova Gajdosova,[35] M. Kroesen,[94] M. Krüger,[63] D. M. Krupova,[35] E. Kryshen,[140] V. Kučera,[32] C. Kuhn,[127] P. G. Kuijer,[84] T. Kumaoka,[123] D. Kumar,[132] L. Kumar,[90] N. Kumar,[90] S. Kumar,[31] S. Kundu,[32] P. Kurashvili,[79] A. Kurepin,[140] A. B. Kurepin,[140] A. Kuryakin,[140] S. Kushpil,[86] J. Kvapil,[100] M. J. Kweon,[57] J. Y. Kwon,[57] Y. Kwon,[138] S. L. La Pointe,[38] P. La Rocca,[26] Y. S. Lai,[74] A. Lakrathok,[105] M. Lamanna,[32] R. Langoy,[119] P. Larionov,[32] E. Laudi,[32] L. Lautner,[32,95] R. Lavicka,[102] T. Lazareva,[140] R. Lea,[131,54] H. Lee,[104] G. Legras,[135] J. Lehrbach,[38] R. C. Lemmon,[85] I. León Monzón,[109] M. M. Lesch,[95] E. D. Lesser,[18] M. Lettrich,[95] P. Lévai,[136] X. Li,[10] X. L. Li,[6] J. Lien,[119] R. Lietava,[100] B. Lim,[24,16] S. H. Lim,[16] V. Lindenstruth,[38] A. Lindner,[45] C. Lippmann,[97] A. Liu,[18] D. H. Liu,[6] J. Liu,[117] I. M. Lofnes,[20] C. Loizides,[87] S. Lokos,[107] P. Loncar,[33] J. A. Lopez,[94] X. Lopez,[125] E. López Torres,[7] P. Lu,[97,118] J. R. Luhder,[135] M. Lunardon,[27] G. Luparello,[56] Y. G. Ma,[39] A. Maevskaya,[140] M. Mager,[32] T. Mahmoud,[42] A. Maire,[127] M. V. Makariev,[36] M. Malaev,[140] G. Malfattore,[25] N. M. Malik,[91] Q. W. Malik,[19] S. K. Malik,[91] L. Malinina,[141,‖] D. Mal'Kevich,[140] D. Mallick,[80] N. Mallick,[47] G. Mandaglio,[30,52] V. Manko,[140] F. Manso,[125] V. Manzari,[49] Y. Mao,[6] G. V. Margagliotti,[23] A. Margotti,[50] A. Marín,[97] C. Markert,[108] P. Martinengo,[32] J. L. Martinez,[114] M. I. Martínez,[44] G. Martínez García,[103] S. Masciocchi,[97] M. Masera,[24] A. Masoni,[51] L. Massacrier,[72] A. Mastroserio,[129,49] A. M. Mathis,[95] O. Matonoha,[75] P. F. T. Matuoka,[110] A. Matyja,[107] C. Mayer,[107] A. L. Mazuecos,[32] F. Mazzaschi,[24] M. Mazzilli,[32] J. E. Mdhluli,[121] A. F. Mechler,[63] Y. Melikyan,[43,140] A. Menchaca-Rocha,[66] E. Meninno,[102,28] A. S. Menon,[114] M. Meres,[12] S. Mhlanga,[113,67] Y. Miake,[123] L. Micheletti,[55] L. C. Migliorin,[126] D. L. Mihaylov,[95] K. Mikhaylov,[141,140] A. N. Mishra,[136] D. Miśkowiec,[97] A. Modak,[4] A. P. Mohanty,[58] B. Mohanty,[80] M. Mohisin Khan,[15,¶] M. A. Molander,[43] Z. Moravcova,[83] C. Mordasini,[95] D. A. Moreira De Godoy,[135] I. Morozov,[140] A. Morsch,[32] T. Mrnjavac,[32] V. Muccifora,[48] S. Muhuri,[132] J. D. Mulligan,[74] A. Mulliri,[22] M. G. Munhoz,[110] R. H. Munzer,[63] H. Murakami,[122] S. Murray,[113] L. Musa,[32] J. Musinsky,[59] J. W. Myrcha,[133] B. Naik,[121] A. I. Nambrath,[18] B. K. Nandi,[46] R. Nania,[50] E. Nappi,[49] A. F. Nassirpour,[75] A. Nath,[94] C. Nattrass,[120] M. N. Naydenov,[36] A. Neagu,[19] A. Negru,[124] L. Nellen,[64] S. V. Nesbo,[34] G. Neskovic,[38] D. Nesterov,[140] B. S. Nielsen,[83] E. G. Nielsen,[83] S. Nikolaev,[140] S. Nikulin,[140] V. Nikulin,[140] F. Noferini,[50] S. Noh,[11] P. Nomokonov,[141] J. Norman,[117] N. Novitzky,[123] P. Nowakowski,[133] A. Nyanin,[140] J. Nystrand,[20] M. Ogino,[76] A. Ohlson,[75] V. A. Okorokov,[140] J. Oleniacz,[133] A. C. Oliveira Da Silva,[120] M. H. Oliver,[137] A. Onnerstad,[115] C. Oppedisano,[55] A. Ortiz Velasquez,[64] J. Otwinowski,[107] M. Oya,[92] K. Oyama,[76] Y. Pachmayer,[94] S. Padhan,[46] D. Pagano,[131,54] G. Paić,[64] A. Palasciano,[49] S. Panebianco,[128] H. Park,[123] H. Park,[104] J. Park,[57] J. E. Parkkila,[32] R. N. Patra,[91] B. Paul,[22] H. Pei,[6] T. Peitzmann,[58] X. Peng,[6] M. Pennisi,[24] L. G. Pereira,[65] D. Peresunko,[140] G. M. Perez,[7] S. Perrin,[128] Y. Pestov,[140] V. Petráček,[35] V. Petrov,[140] M. Petrovici,[45] R. P. Pezzi,[103,65] S. Piano,[56] M. Pikna,[12] P. Pillot,[103] O. Pinazza,[50,32] L. Pinsky,[114] C. Pinto,[95] S. Pisano,[48] M. Płoskoń,[74] M. Planinic,[89] F. Pliquett,[63] M. G. Poghosyan,[87] B. Polichtchouk,[140] S. Politano,[29]

N. Poljak,[89] A. Pop,[45] S. Porteboeuf-Houssais,[125] V. Pozdniakov,[141] K. K. Pradhan,[47] S. K. Prasad,[4] S. Prasad,[47] R. Preghenella,[50] F. Prino,[55] C. A. Pruneau,[134] I. Pshenichnov,[140] M. Puccio,[32] S. Pucillo,[24] Z. Pugelova,[106] S. Qiu,[84] L. Quaglia,[24] R. E. Quishpe,[114] S. Ragoni,[14,100] A. Rakotozafindrabe,[128] L. Ramello,[130,55] F. Rami,[127] S. A. R. Ramirez,[44] T. A. Rancien,[73] M. Rasa,[26] S. S. Räsänen,[43] R. Rath,[50,47] M. P. Rauch,[20] I. Ravasenga,[84] K. F. Read,[87,120] C. Reckziegel,[112] A. R. Redelbach,[38] K. Redlich,[79,**] A. Rehman,[20] F. Reidt,[32] H. A. Reme-Ness,[34] Z. Rescakova,[37] K. Reygers,[94] A. Riabov,[140] V. Riabov,[140] R. Ricci,[28] M. Richter,[19] A. A. Riedel,[95] W. Riegler,[32] C. Ristea,[62] S. P. Rode,[141] M. Rodríguez Cahuantzi,[44] K. Røed,[19] R. Rogalev,[140] E. Rogochaya,[141] T. S. Rogoschinski,[63] D. Rohr,[32] D. Röhrich,[20] P. F. Rojas,[44] S. Rojas Torres,[35] P. S. Rokita,[133] G. Romanenko,[141] F. Ronchetti,[48] A. Rosano,[30,52] E. D. Rosas,[64] A. Rossi,[53] A. Roy,[47] S. Roy,[46] N. Rubini,[25] O. V. Rueda,[114,75] D. Ruggiano,[133] R. Rui,[23] B. Rumyantsev,[141] P. G. Russek,[2] R. Russo,[84] A. Rustamov,[81] E. Ryabinkin,[140] Y. Ryabov,[140] A. Rybicki,[107] H. Rytkonen,[115] W. Rzesa,[133] O. A. M. Saarimaki,[43] R. Sadek,[103] S. Sadhu,[31] S. Sadovsky,[140] J. Saetre,[20] K. Šafařík,[35] S. K. Saha,[4] S. Saha,[80] B. Sahoo,[46] R. Sahoo,[47] S. Sahoo,[60] D. Sahu,[47] P. K. Sahu,[60] J. Saini,[132] K. Sajdakova,[37] S. Sakai,[123] M. P. Salvan,[97] S. Sambyal,[91] I. Sanna,[32,95] T. B. Saramela,[110] D. Sarkar,[134] N. Sarkar,[132] P. Sarma,[41] V. Sarritzu,[22] V. M. Sarti,[95] M. H. P. Sas,[137] J. Schambach,[87] H. S. Scheid,[63] C. Schiaua,[45] R. Schicker,[94] A. Schmah,[94] C. Schmidt,[97] H. R. Schmidt,[93] M. O. Schmidt,[32] M. Schmidt,[93] N. V. Schmidt,[87] A. R. Schmier,[120] R. Schotter,[127] A. Schröter,[38] J. Schukraft,[32] K. Schwarz,[97] K. Schweda,[97] G. Scioli,[25] E. Scomparin,[55] J. E. Seger,[14] Y. Sekiguchi,[122] D. Sekihata,[122] I. Selyuzhenkov,[97,140] S. Senyukov,[127] J. J. Seo,[57] D. Serebryakov,[140] L. Šerkšnytė,[95] A. Sevcenco,[62] T. J. Shaba,[67] A. Shabetai,[103] R. Shahoyan,[32] A. Shangaraev,[140] A. Sharma,[90] B. Sharma,[91] D. Sharma,[46] H. Sharma,[107] M. Sharma,[91] S. Sharma,[76] S. Sharma,[91] U. Sharma,[91] A. Shatat,[72] O. Sheibani,[114] K. Shigaki,[92] M. Shimomura,[77] J. Shin,[11] S. Shirinkin,[140] Q. Shou,[39] Y. Sibiriak,[140] S. Siddhanta,[51] T. Siemiarczuk,[79] T. F. Silva,[110] D. Silvermyr,[75] T. Simantathammakul,[105] R. Simeonov,[36] B. Singh,[91] B. Singh,[95] R. Singh,[80] R. Singh,[91] R. Singh,[47] S. Singh,[15] V. K. Singh,[132] V. Singhal,[132] T. Sinha,[99] B. Sitar,[12] M. Sitta,[130,55] T. B. Skaali,[19] G. Skorodumovs,[94] M. Slupecki,[43] N. Smirnov,[137] R. J. M. Snellings,[58] E. H. Solheim,[19] J. Song,[114] A. Songmoolnak,[105] F. Soramel,[27] R. Spijkers,[84] I. Sputowska,[107] J. Staa,[75] J. Stachel,[94] I. Stan,[62] P. J. Steffanic,[120] S. F. Stiefelmaier,[94] D. Stocco,[103] I. Storehaug,[19] P. Stratmann,[135] S. Strazzi,[25] C. P. Stylianidis,[84] A. A. P. Suaide,[110] C. Suire,[72] M. Sukhanov,[140] M. Suljic,[32] R. Sultanov,[140] V. Sumberia,[91] S. Sumowidagdo,[82] S. Swain,[60] I. Szarka,[12] S. F. Taghavi,[95] G. Taillepied,[97] J. Takahashi,[111] G. J. Tambave,[20] S. Tang,[125,6] Z. Tang,[118] J. D. Tapia Takaki,[116] N. Tapus,[124] L. A. Tarasovicova,[135] M. G. Tarzila,[45] G. F. Tassielli,[31] A. Tauro,[32] G. Tejeda Muñoz,[44] A. Telesca,[32] L. Terlizzi,[24] C. Terrevoli,[114] G. Tersimonov,[3] S. Thakur,[4] D. Thomas,[108] A. Tikhonov,[140] A. R. Timmins,[114] M. Tkacik,[106] T. Tkacik,[106] A. Toia,[63] R. Tokumoto,[92] N. Topilskaya,[140] M. Toppi,[48] F. Torales-Acosta,[18] T. Tork,[72] A. G. Torres Ramos,[31] A. Trifiró,[30,52] A. S. Triolo,[30,52] S. Tripathy,[50] T. Tripathy,[46] S. Trogolo,[32] V. Trubnikov,[3] W. H. Trzaska,[115] T. P. Trzcinski,[133] A. Tumkin,[140] R. Turrisi,[53] T. S. Tveter,[19] K. Ullaland,[20] B. Ulukutlu,[95] A. Uras,[126] M. Urioni,[54,131] G. L. Usai,[22] M. Vala,[37] N. Valle,[21] L. V. R. van Doremalen,[58] M. van Leeuwen,[84] C. A. van Veen,[94] R. J. G. van Weelden,[84] P. Vande Vyvre,[32] D. Varga,[136] Z. Varga,[136] M. Vasileiou,[78] A. Vasiliev,[140] O. Vázquez Doce,[48] V. Vechernin,[140] E. Vercellin,[24] S. Vergara Limón,[44] L. Vermunt,[97] R. Vértesi,[136] M. Verweij,[58] L. Vickovic,[33] Z. Vilakazi,[121] O. Villalobos Baillie,[100] G. Vino,[49] A. Vinogradov,[140] T. Virgili,[28] V. Vislavicius,[83] A. Vodopyanov,[141] B. Volkel,[32] M. A. Völkl,[94] K. Voloshin,[140] S. A. Voloshin,[134] G. Volpe,[31] B. von Haller,[32] I. Vorobyev,[95] N. Vozniuk,[140] J. Vrláková,[37] C. Wang,[39] D. Wang,[39] Y. Wang,[39] A. Wegrzynek,[32] F. T. Weiglhofer,[38] S. C. Wenzel,[32] J. P. Wessels,[135] S. L. Weyhmiller,[137] J. Wiechula,[63] J. Wikne,[19] G. Wilk,[79] J. Wilkinson,[97] G. A. Willems,[135] B. Windelband,[94] M. Winn,[128] J. R. Wright,[108] W. Wu,[39] Y. Wu,[118] R. Xu,[6] A. Yadav,[42] A. K. Yadav,[132] S. Yalcin,[71] Y. Yamaguchi,[92] K. Yamakawa,[92] S. Yang,[20] S. Yano,[92] Z. Yin,[6] I.-K. Yoo,[16] J. H. Yoon,[57] S. Yuan,[20] A. Yuncu,[94] V. Zaccolo,[23] C. Zampolli,[32] F. Zanone,[94] N. Zardoshti,[32,100] A. Zarochentsev,[140] P. Závada,[61] N. Zaviyalov,[140] M. Zhalov,[140] B. Zhang,[6] L. Zhang,[39] S. Zhang,[39] X. Zhang,[6] Y. Zhang,[118] Z. Zhang,[6] M. Zhao,[10] V. Zherebchevskii,[140] Y. Zhi,[10] D. Zhou,[6] Y. Zhou,[83] J. Zhu,[97,6] Y. Zhu,[6] S. C. Zugravel,[55] and N. Zurlo[131,54]

(ALICE Collaboration)

[1]*A.I. Alikhanyan National Science Laboratory (Yerevan Physics Institute) Foundation, Yerevan, Armenia*
[2]*AGH University of Science and Technology, Cracow, Poland*
[3]*Bogolyubov Institute for Theoretical Physics, National Academy of Sciences of Ukraine, Kiev, Ukraine*
[4]*Bose Institute, Department of Physics and Centre for Astroparticle Physics and Space Science (CAPSS), Kolkata, India*
[5]*California Polytechnic State University, San Luis Obispo, California, USA*
[6]*Central China Normal University, Wuhan, China*
[7]*Centro de Aplicaciones Tecnológicas y Desarrollo Nuclear (CEADEN), Havana, Cuba*
[8]*Centro de Investigación y de Estudios Avanzados (CINVESTAV), Mexico City and Mérida, Mexico*
[9]*Chicago State University, Chicago, Illinois, USA*

[10]*China Institute of Atomic Energy, Beijing, China*
[11]*Chungbuk National University, Cheongju, Republic of Korea*
[12]*Comenius University Bratislava, Faculty of Mathematics, Physics and Informatics, Bratislava, Slovak Republic*
[13]*COMSATS University Islamabad, Islamabad, Pakistan*
[14]*Creighton University, Omaha, Nebraska, USA*
[15]*Department of Physics, Aligarh Muslim University, Aligarh, India*
[16]*Department of Physics, Pusan National University, Pusan, Republic of Korea*
[17]*Department of Physics, Sejong University, Seoul, Republic of Korea*
[18]*Department of Physics, University of California, Berkeley, California, USA*
[19]*Department of Physics, University of Oslo, Oslo, Norway*
[20]*Department of Physics and Technology, University of Bergen, Bergen, Norway*
[21]*Dipartimento di Fisica, Università di Pavia, Pavia, Italy*
[22]*Dipartimento di Fisica dell'Università and Sezione INFN, Cagliari, Italy*
[23]*Dipartimento di Fisica dell'Università and Sezione INFN, Trieste, Italy*
[24]*Dipartimento di Fisica dell'Università and Sezione INFN, Turin, Italy*
[25]*Dipartimento di Fisica e Astronomia dell'Università and Sezione INFN, Bologna, Italy*
[26]*Dipartimento di Fisica e Astronomia dell'Università and Sezione INFN, Catania, Italy*
[27]*Dipartimento di Fisica e Astronomia dell'Università and Sezione INFN, Padova, Italy*
[28]*Dipartimento di Fisica 'E.R. Caianiello' dell'Università and Gruppo Collegato INFN, Salerno, Italy*
[29]*Dipartimento DISAT del Politecnico and Sezione INFN, Turin, Italy*
[30]*Dipartimento di Scienze MIFT, Università di Messina, Messina, Italy*
[31]*Dipartimento Interateneo di Fisica 'M. Merlin' and Sezione INFN, Bari, Italy*
[32]*European Organization for Nuclear Research (CERN), Geneva, Switzerland*
[33]*Faculty of Electrical Engineering, Mechanical Engineering and Naval Architecture, University of Split, Split, Croatia*
[34]*Faculty of Engineering and Science, Western Norway University of Applied Sciences, Bergen, Norway*
[35]*Faculty of Nuclear Sciences and Physical Engineering, Czech Technical University in Prague, Prague, Czech Republic*
[36]*Faculty of Physics, Sofia University, Sofia, Bulgaria*
[37]*Faculty of Science, P.J. Šafárik University, Košice, Slovak Republic*
[38]*Frankfurt Institute for Advanced Studies, Johann Wolfgang Goethe-Universität Frankfurt, Frankfurt, Germany*
[39]*Fudan University, Shanghai, China*
[40]*Gangneung-Wonju National University, Gangneung, Republic of Korea*
[41]*Gauhati University, Department of Physics, Guwahati, India*
[42]*Helmholtz-Institut für Strahlen- und Kernphysik, Rheinische Friedrich-Wilhelms-Universität Bonn, Bonn, Germany*
[43]*Helsinki Institute of Physics (HIP), Helsinki, Finland*
[44]*High Energy Physics Group, Universidad Autónoma de Puebla, Puebla, Mexico*
[45]*Horia Hulubei National Institute of Physics and Nuclear Engineering, Bucharest, Romania*
[46]*Indian Institute of Technology Bombay (IIT), Mumbai, India*
[47]*Indian Institute of Technology Indore, Indore, India*
[48]*INFN, Laboratori Nazionali di Frascati, Frascati, Italy*
[49]*INFN, Sezione di Bari, Bari, Italy*
[50]*INFN, Sezione di Bologna, Bologna, Italy*
[51]*INFN, Sezione di Cagliari, Cagliari, Italy*
[52]*INFN, Sezione di Catania, Catania, Italy*
[53]*INFN, Sezione di Padova, Padova, Italy*
[54]*INFN, Sezione di Pavia, Pavia, Italy*
[55]*INFN, Sezione di Torino, Turin, Italy*
[56]*INFN, Sezione di Trieste, Trieste, Italy*
[57]*Inha University, Incheon, Republic of Korea*
[58]*Institute for Gravitational and Subatomic Physics (GRASP), Utrecht University/Nikhef, Utrecht, Netherlands*
[59]*Institute of Experimental Physics, Slovak Academy of Sciences, Košice, Slovak Republic*
[60]*Institute of Physics, Homi Bhabha National Institute, Bhubaneswar, India*
[61]*Institute of Physics of the Czech Academy of Sciences, Prague, Czech Republic*
[62]*Institute of Space Science (ISS), Bucharest, Romania*
[63]*Institut für Kernphysik, Johann Wolfgang Goethe-Universität Frankfurt, Frankfurt, Germany*
[64]*Instituto de Ciencias Nucleares, Universidad Nacional Autónoma de México, Mexico City, Mexico*
[65]*Instituto de Física, Universidade Federal do Rio Grande do Sul (UFRGS), Porto Alegre, Brazil*
[66]*Instituto de Física, Universidad Nacional Autónoma de México, Mexico City, Mexico*
[67]*iThemba LABS, National Research Foundation, Somerset West, South Africa*
[68]*Jeonbuk National University, Jeonju, Republic of Korea*

[69]*Johann-Wolfgang-Goethe Universität Frankfurt Institut für Informatik, Fachbereich Informatik und Mathematik, Frankfurt, Germany*
[70]*Korea Institute of Science and Technology Information, Daejeon, Republic of Korea*
[71]*KTO Karatay University, Konya, Turkey*
[72]*Laboratoire de Physique des 2 Infinis, Irène Joliot-Curie, Orsay, France*
[73]*Laboratoire de Physique Subatomique et de Cosmologie, Université Grenoble-Alpes, CNRS-IN2P3, Grenoble, France*
[74]*Lawrence Berkeley National Laboratory, Berkeley, California, USA*
[75]*Lund University Department of Physics, Division of Particle Physics, Lund, Sweden*
[76]*Nagasaki Institute of Applied Science, Nagasaki, Japan*
[77]*Nara Women's University (NWU), Nara, Japan*
[78]*National and Kapodistrian University of Athens, School of Science, Department of Physics, Athens, Greece*
[79]*National Centre for Nuclear Research, Warsaw, Poland*
[80]*National Institute of Science Education and Research, Homi Bhabha National Institute, Jatni, India*
[81]*National Nuclear Research Center, Baku, Azerbaijan*
[82]*National Research and Innovation Agency - BRIN, Jakarta, Indonesia*
[83]*Niels Bohr Institute, University of Copenhagen, Copenhagen, Denmark*
[84]*Nikhef, National institute for subatomic physics, Amsterdam, Netherlands*
[85]*Nuclear Physics Group, STFC Daresbury Laboratory, Daresbury, United Kingdom*
[86]*Nuclear Physics Institute of the Czech Academy of Sciences, Husinec-Řež, Czech Republic*
[87]*Oak Ridge National Laboratory, Oak Ridge, Tennessee, USA*
[88]*Ohio State University, Columbus, Ohio, USA*
[89]*Physics department, Faculty of science, University of Zagreb, Zagreb, Croatia*
[90]*Physics Department, Panjab University, Chandigarh, India*
[91]*Physics Department, University of Jammu, Jammu, India*
[92]*Physics Program and International Institute for Sustainability with Knotted Chiral Meta Matter (SKCM2), Hiroshima University, Hiroshima, Japan*
[93]*Physikalisches Institut, Eberhard-Karls-Universität Tübingen, Tübingen, Germany*
[94]*Physikalisches Institut, Ruprecht-Karls-Universität Heidelberg, Heidelberg, Germany*
[95]*Physik Department, Technische Universität München, Munich, Germany*
[96]*Politecnico di Bari and Sezione INFN, Bari, Italy*
[97]*Research Division and ExtreMe Matter Institute EMMI, GSI Helmholtzzentrum für Schwerionenforschung GmbH, Darmstadt, Germany*
[98]*Saga University, Saga, Japan*
[99]*Saha Institute of Nuclear Physics, Homi Bhabha National Institute, Kolkata, India*
[100]*School of Physics and Astronomy, University of Birmingham, Birmingham, United Kingdom*
[101]*Sección Física, Departamento de Ciencias, Pontificia Universidad Católica del Perú, Lima, Peru*
[102]*Stefan Meyer Institut für Subatomare Physik (SMI), Vienna, Austria*
[103]*SUBATECH, IMT Atlantique, Nantes Université, CNRS-IN2P3, Nantes, France*
[104]*Sungkyunkwan University, Suwon City, Republic of Korea*
[105]*Suranaree University of Technology, Nakhon Ratchasima, Thailand*
[106]*Technical University of Košice, Košice, Slovak Republic*
[107]*The Henryk Niewodniczanski Institute of Nuclear Physics, Polish Academy of Sciences, Cracow, Poland*
[108]*The University of Texas at Austin, Austin, Texas, USA*
[109]*Universidad Autónoma de Sinaloa, Culiacán, Mexico*
[110]*Universidade de São Paulo (USP), São Paulo, Brazil*
[111]*Universidade Estadual de Campinas (UNICAMP), Campinas, Brazil*
[112]*Universidade Federal do ABC, Santo Andre, Brazil*
[113]*University of Cape Town, Cape Town, South Africa*
[114]*University of Houston, Houston, Texas, USA*
[115]*University of Jyväskylä, Jyväskylä, Finland*
[116]*University of Kansas, Lawrence, Kansas, USA*
[117]*University of Liverpool, Liverpool, United Kingdom*
[118]*University of Science and Technology of China, Hefei, China*
[119]*University of South-Eastern Norway, Kongsberg, Norway*
[120]*University of Tennessee, Knoxville, Tennessee, USA*
[121]*University of the Witwatersrand, Johannesburg, South Africa*
[122]*University of Tokyo, Tokyo, Japan*
[123]*University of Tsukuba, Tsukuba, Japan*
[124]*University Politehnica of Bucharest, Bucharest, Romania*
[125]*Université Clermont Auvergne, CNRS/IN2P3, LPC, Clermont-Ferrand, France*
[126]*Université de Lyon, CNRS/IN2P3, Institut de Physique des 2 Infinis de Lyon, Lyon, France*

[127] *Université de Strasbourg, CNRS, IPHC UMR 7178, F-67000 Strasbourg, France, Strasbourg, France*
[128] *Université Paris-Saclay Centre d'Etudes de Saclay (CEA), IRFU, Départment de Physique Nucléaire (DPhN), Saclay, France*
[129] *Università degli Studi di Foggia, Foggia, Italy*
[130] *Università del Piemonte Orientale, Vercelli, Italy*
[131] *Università di Brescia, Brescia, Italy*
[132] *Variable Energy Cyclotron Centre, Homi Bhabha National Institute, Kolkata, India*
[133] *Warsaw University of Technology, Warsaw, Poland*
[134] *Wayne State University, Detroit, Michigan, USA*
[135] *Westfälische Wilhelms-Universität Münster, Institut für Kernphysik, Münster, Germany*
[136] *Wigner Research Centre for Physics, Budapest, Hungary*
[137] *Yale University, New Haven, Connecticut, USA*
[138] *Yonsei University, Seoul, Republic of Korea*
[139] *Zentrum für Technologie und Transfer (ZTT), Worms, Germany*
[140] *Affiliated with an institute covered by a cooperation agreement with CERN*
[141] *Affiliated with an international laboratory covered by a cooperation agreement with CERN*

[*] Also at Max-Planck-Institut für Physik, Munich, Germany.
[†] Also at Italian National Agency for New Technologies, Energy and Sustainable Economic Development (ENEA), Bologna, Italy.
[‡] Also at Dipartimento DET del Politecnico di Torino, Turin, Italy.
[§] Deceased.
[‖] Also at An institution covered by a cooperation agreement with CERN.
[¶] Also at Department of Applied Physics, Aligarh Muslim University, Aligarh, India.
[**] Also at Institute of Theoretical Physics, University of Wroclaw, Poland.